Four-Dimensional paleomagnetic dataset: Late Neogene paleodirection and paleointensity results from the Erebus Volcanic Province, Antarctica

Hanna Asefaw[1], Lisa Tauxe[2], Anthony A.P. Koppers[3], and Hubert Staudigel[2]

[1]Scripps Institution of Oceanography, University of California San Diego, USA
[2]University of California, San Diego
[3]Oregon State University

November 22, 2022

Abstract

A fundamental assumption in paleomagnetism is that a geocentric axial dipole (GAD) geomagnetic field structure extends to the ancient field. Global paleodirectional compilations that span 0 - 10 Myr support a GAD dominated field structure with minor non-GAD contributions, however, the paleointensity data over the same period do not. In a GAD field, higher latitudes should preserve higher intensity, but the current database suggests that intensities are independent of latitude. To determine whether the seemingly "low' intensities from Antarctica reflect the ancient field, rather than low quality data or inadequate temporal sampling, we have conducted a new study of the paleomagnetic field in Antarctica. This study focuses on the paleomagnetic field structure over the Late Neogene. We combine and re-analyze new and published paleodirectional and paleointensity results from the Erebus volcanic province to recover directions from 107 sites that were both thermally and AF demagnetized and then subjected to a set of strict selection criteria and 28 paleointensity estimates from specimens that underwent the IZZI modified Thellier-Thellier experiment and were also subjected to a strict set of selection criteria. The paleopole (205.6°, 87.1°) and α_{95} (5.5°) recovered from our paleodirectional study supports the GAD hypothesis and the scatter of the virtual geomagnetic poles is within the uncertainty of that predicted by TK03 paleosecular variation model. Our time averaged field strength estimate, 33.01 μT $\pm$ 2.59 μT, is significantly lower than that expected for a GAD field estimated from the present field, but consistent with the long term average field.

Four-Dimensional paleomagnetic dataset: Late Neogene paleodirection and paleointensity results from the Erebus Volcanic Province, Antarctica

H. A. Asefaw[1], L. Tauxe[1], A.A.P. Koppers[2], H. Staudigel[1]

[1]Geosciences Research Division, Scripps Institution of Oceanography, University of California San Diego, La Jolla, California, USA
[2]College of Earth, Ocean and Atmospheric Sciences, Oregon State University, Corvallis, Oregon, USA,

Key Points:

- We present 11 new $^{40}Ar/^{39}Ar$ age determinations from the Erebus Volcanic Province, Antarctica (-78°, 167°).
- We present 107 high quality site directions resulting in VGP scatter consistent with model predictions and a paleopole consistent with GAD.
- We present 28 new paleointensities that yield an estimated average dipole moment of 43± 3.4 ZAm^2.

Plain Language Summary

The GAD hypothesis states that the Earth's magnetic field may be approximated by an Earth-centric dipole aligned with the rotation axis. This hypothesis is fundamental for paleogeographic reconstructions of the tectonic plates. While global paleomagnetic directions from the last 10 Myrs recover a predominately GAD field structure, paleointensity estimates over the same time period do not. In this study, we re-examine the paleomagnetic field structure in the Erebus Volcanic Province, Antarctica, and recover a robust dataset of directional and intensity data. We then compare the paleopole and average dipole moment against a GAD field structure and model predictions of paleosecular variation.

Corresponding author: Hanna Asefaw, `hasafaw@ucsd.edu`

Abstract

A fundamental assumption in paleomagnetism is that a geocentric axial dipole (GAD) geomagnetic field structure extends to the ancient field. Global paleodirectional compilations that span 0 - 10 Myr support a GAD dominated field structure with minor non-GAD contributions, however, the paleointensity data over the same period do not. In a GAD field, higher latitudes should preserve higher intensity, but the current database suggests that intensities are independent of latitude. To determine whether the seemingly "low" intensities from Antarctica reflect the ancient field, rather than low quality data or inadequate temporal sampling, we have conducted a new study of the paleomagnetic field in Antarctica. This study focuses on the paleomagnetic field structure over the Late Neogene. We combine and re-analyze new and published paleodirectional and paleointensity results from the Erebus volcanic province to recover directions from 107 sites that were both thermally and AF demagnetized and then subjected to a set of strict selection criteria and 28 paleointensity estimates from specimens that underwent the IZZI modified Thellier-Thellier experiment and were also subjected to a strict set of selection criteria. The paleopole (205.6 °, 87.1°) and α_{95} (5.5°) recovered from our paleodirectional study supports the GAD hypothesis and the scatter of the virtual geomagnetic poles is within the uncertainty of that predicted by TK03 paleosecular variation model. Our time averaged field strength estimate, 33.01 μT $\pm$ 2.59 μT, is significantly lower than that expected for a GAD field estimated from the present field, but consistent with the long term average field.

1 Introduction

A geocentric axial dipole (GAD) field is the magnetic field generated by a dipole that is positioned in the center of the Earth and aligned along the spin axis (Gilbert, 1958). In mathematical representations of the geomagnetic field structure, such as the International Geomagnetic Reference Field (IGRF), the axial dipole term (g_1^0) accounts for the majority of the field (Lowes, 1973). However, modern geomagnetic field strengths around the globe (Figure 1a) reveal latitudinal and longitudinal non-GAD features and regions with anomalously low (e.g. the South Atlantic Anomaly, or SAA) and high (e.g. south of Australia) intensities. It is frequently assumed (e.g., (McElhinny, 2007) that the field, when averaged over sufficient time, is well approximated by a GAD field. Given a GAD field (Figure 1b) both the intensity of the geomagnetic field (B) and the inclination (I) would vary with latitude (λ) by:

$$B = M\sqrt{1 + 3\cos^2(\frac{\pi}{2} - \lambda)} \tag{1}$$

and

$$\tan(I) = 2\tan(\lambda) \tag{2}$$

where M is the g_1^0 term in nT (and also the intensity of the field at the equator).

Both the GAD and non-GAD terms of the geomagnetic field vary with time, a phenomenon known as secular variation. The terms of the IGRF have been estimated for the last century or so (Thébault et al., 2015), using geomagnetic observatory and, more recently, satellite data. From 1600 to modern geomagnetic observatories, IGRF-like models were based on ship-board measurement data (Jackson et al., 2000). Prior to about 1600, measurements of the geomagnetic field are too scare for constraining reference models and so we rely on geologic and archaeologic materials (e.g., Constable et al. (2016) and references therein). The paleomagnetic field structure can be preserved in the geological record and various techniques allow us to the recover paleodirections (Irving et al., 1961; Creer, 1967; Stephenson, 1967) and paleointensities (Thellier & Thellier, 1959; Shaw, 1974; Coe, 1967; Yu et al., 2004; Walton & Shaw, 1922; Hoffman & Biggin, 2005). Independent studies of the paleofield are then compiled into paleomagnetic databases (e.g., the MagIC database at: earthref.org/MagIC). We can then use these data to characterize the behavior of paleosecular variation (PSV) and the time averaged field (TAF). Changes in the structure of the geomagnetic field at the surface of the Earth reflect the dynamics occurring in the fluid outer core (Glatzmaier & Coe, 2007; Jackson & Finlay, 2007; Holme, 2007; Livermore et al., 2014) so an accurate characterization of the field is important for understanding the outer core.

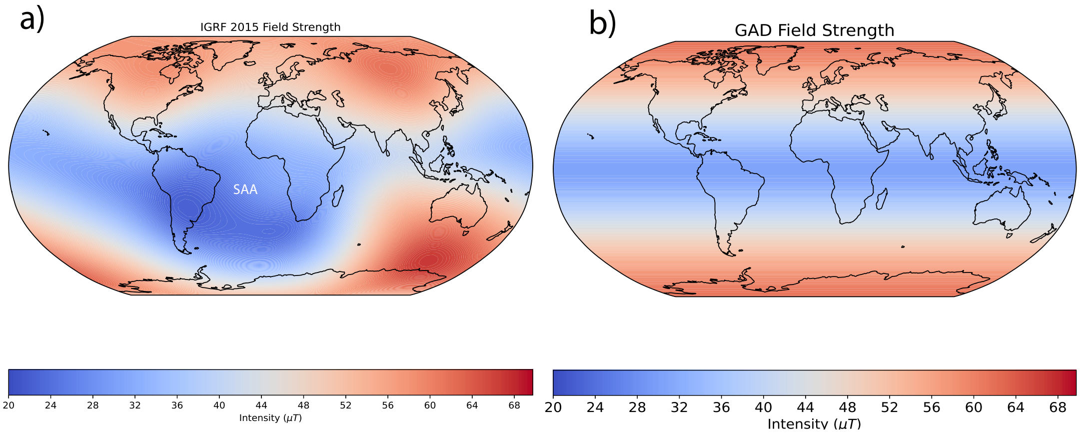

Figure 1. a) Intensity of the geomagnetic field estimated from the 2015 IGRF model. b) Intensity of the geomagnetic field expected for a GAD field with an 80 ZAm^2 magnetic moment.

Numerous studies (Opdyke & Henry, 1969; McElhinny & Lock, 1996; Johnson et al., 2008; Cromwell, Tauxe, et al., 2018; Behar et al., 2019) have recovered paleodirections from the Neogene that are largely consistent with a GAD field with small non-GAD terms. Early compilations of absolute paleointensities were also interpreted as largely consistent with a GAD structure (McFadden & Mcelhinny, 1982; Tanaka et al., 1995) with a paleomagnetic dipole moment (PDM) similar to the present dipole moment of $\sim$80 ZAm^2. When considering data from submarine basaltic glass over the last five million years, Selkin and Tauxe (2000) found a reasonable fit to intensities predicted by a PDM of $\sim$45 ZAm^2. However, the dipole signature is not evident in modern absolute paleointensity databases, which include data from a variety of materials and methods (e.g., PINT15 of Biggin (2010) and the MagIC database at https://earthref.org/MagIC) over the same time period (Lawrence et al., 2009; Tauxe & Yamazaki, 2015; Wang et al., 2015), see Figure 2). The lack of a dipole signal in the current global database may reflect a paleomagnetic field structure with stronger non-GAD components than previously recognized or a bias in the global data set as a consequence of poor temporal sampling, poor experimental design or poor choice of sample materials. Therefore, the reliability of the data from high southerly latitudes is key to understanding the behavior of the geomagnetic field.

Recovering paleointensity is challenging owing to the complex magnetization acquisition behavior of non-ideal magnetic grains (Dunlop et al., 2005; Dunlop & Özdemir, 2001; Tauxe & Yamazaki, 2015) and the tendency for magnetomineralogical alteration during paleointensity experiments (Coe, 1967; Smirnov & Tarduno, 2003). To determine whether the ‘low’ intensities measured at the high southerly latitudes are an artifact of non-ideal magnetic recorders or are in fact an accurate representation of the paleomagnetic field structure, we conducted an extensive study of the paleomagnetic field in the Erebus Volcanic Province, Antarctica (-78°, 167°). Our goal was to target the finest grained (glassiest) material (Selkin & Tauxe, 2000; Cromwell et al., 2015), treat them to a rig-

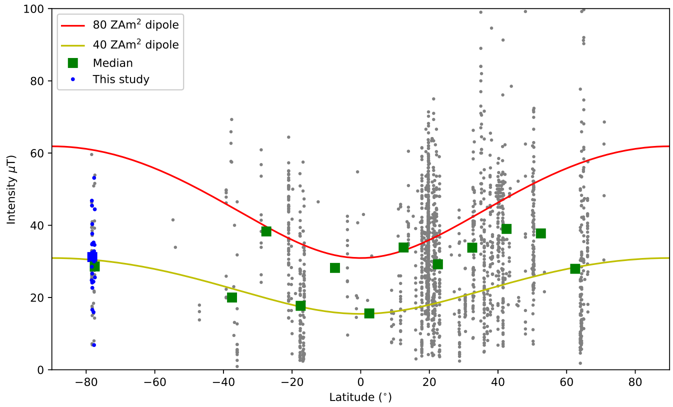

Figure 2. Global paleointensity estimates over the last 5 Myr taken from the PINT15 database (Biggin, 2010) of absolute paleointensities (grey circles). The intensity estimates are binned into 10° latitude intervals. The median value of bins with 10 or more sites is plotted as green squares. The results from this study are marked as blue points along with their median intensity (blue square). The yellow curve (red curve) marks the intensity at a given latitude expected for a dipole moment of 40 ZAm^2 (80 ZAm^2).

orous experimental protocol (Yu et al., 2004) and subject the results to a set of strict selection criteria (Cromwell et al., 2015).

2 Methods

2.1 Sample Collection

Mankinen and Cox (1988) drilled between 6 and 8 oriented core samples from the interior of lava flows around the Erebus Volcanic Province, Antarctica (Figure 3) and reported directions from the natural remanent magnetization (NRM). Tauxe et al. (2004) analyzed the Mankinen/Cox sample collection for directions and intensities. Lawrence et al. (2009) reported on a larger suite of samples collected in two field seasons (2003/2004 and 2005/2006), which included at least 10 cores per lava flow; they compiled all the paleodirectional and paleointensity experiments from these cores and those collected earlier by Mankinen and Cox (1988).

Several recent studies (e.g., Cromwell et al. (2015)) have suggested that finer grained lava flow tops, as opposed to flow interiors, coupled with the use of stricter selection criteria, may result in more accurate and precise estimates of paleointensity. We therefore applied the selection criteria proposed by Cromwell et al. (2015) to reanalyze the paleointensity results of Lawrence et al. (2009). In our reanalysis, only a dozen of the original 41 sites pass the CCRIT criteria. Therefore, in the 2015/2016 field season, we resampled nearly all of the original sites reported by Lawrence et al. (2009) (141 total) for this study, targeting only the surfaces of each lava flow. Where possible, we identified the original sites (Table 3) using the 1-inch drill holes remaining in the outcrop. The remainder were located by GPS coordinates from Lawrence et al. (2009) and approximated from the maps and descriptions in Mankinen and Cox (1988). Once we identified the original sampling sites, we re-sampled the microcrystalline, glassy material from the lava flow top or flow bottom. We collected hand samples using hammers and chisels. The outcrops included lava flows, pillow lavas, and hyaloclastite cones that formed over the Late Neogene. Several sites from the original study recover identical paleodirections and re-examination in the field confirmed that these sites sampled the same lava flow, so in this study, we combine these replicates into single sites (see supporting information Table S1).

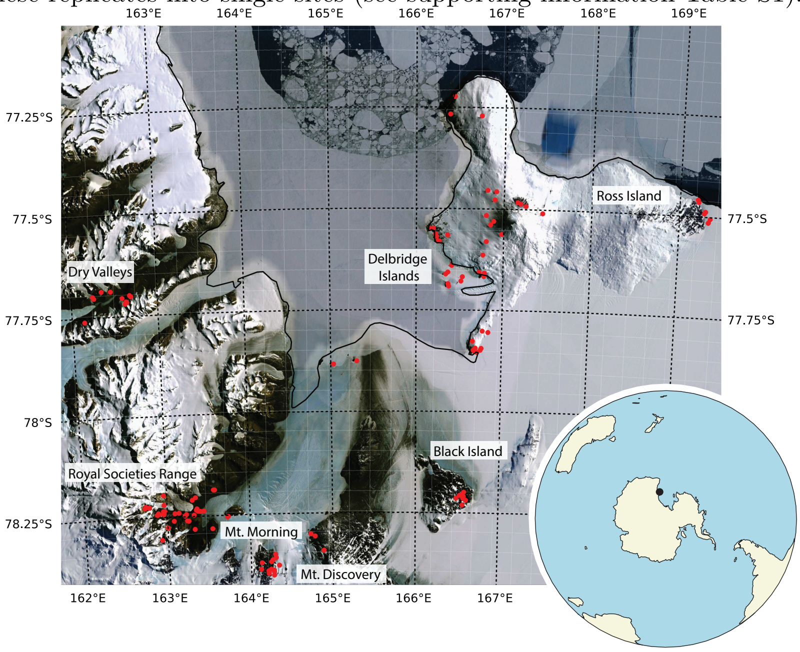

Figure 3. A natural color satellite image of the Erebus Volcanic Province, Antarctica. Our sites (red circles) include the Dry Valleys, Royal Societies Range, Mt. Morning, Mt. Discovery, Black Island, and Ross Island.

2.2 Paleointensity

2.2.1 Recovering paleointensity

Magnetic grains in igneous rocks acquire a thermal remanent magnetization (TRM) by cooling from temperatures well above their Curie temperature through their blocking temperatures (T_b). Once the grain cools below T_b, the resulting TRM captures an instantaneous record of the geomagnetic field that can remain stable over long timescales. The degree of alignment between the magnetic grain moments and the ambient field depends on the strength of the field (B) at the time of cooling (Néel, 1955). For a given population of magnetic grains,

$$M_{TRM} = M_s \tanh \frac{vM_s(T_b)B}{kT_b}, \tag{3}$$

where M_{TRM} is the net magnetization, k is the Boltzmann constant, v is magnetic grain volume, and $M_s(T_b)$ is spontaneous magnetization at T_b.

In a weak magnetic field (of the order of the modern geomagnetic field), TRM acquisition is generally assumed to be quasi-linearly proportional to the strength of the ambient field. This proportionality allows us to recover the intensity of the geomagnetic field when the rock formed. The NRM may be removed by heating the rock and cooling it in zero external field. A new thermal remanent magnetization (TRM) overwrites the NRM by cooling the rock in a controlled field in the laboratory. The ratio of the TRM acquired in the applied field is proportional to the ratio of the NRM acquired in the paleomagnetic field (Néel, 1955). We thus can estimate the intensity of the paleomagnetic field by

$$B_{anc} = \frac{M_{NRM}}{M_{TRM}} B_{lab}, \tag{4}$$

where M_{NRM} is the natural remanent magnetization, B_{lab} is the field applied in the lab, M_{TRM} is the thermal remanent magnetization imparted by heating the specimen, then cooling it in the lab field, and B_{anc} is the strength of the paleomagnetic field. A rock contains an assemblage of magnetic grains and each grain blocks its magnetization at a different temperature. Therefore incrementally demagnetizing and remagnetizing a rock sample at progressively higher temperatures results in several independent estimates of the paleofield, assuming independence of partial TRMs (pTRM) acquired and lost in different temperature intervals.

2.2.2 Specimen preparation

Samples were crushed into 100 – 500 mg fragments. The fragments were then examined under a binocular microscope to select the individual specimens that appeared the freshest and finest grained. These glassy (or microcyrstalline) specimens may contain the single domain grains of magnetite that follow Thellier's laws (Thellier, 1938) and allow us to recover an accurate paleointensity estimate. Each individual specimen was swaddled in glass microfiber filter paper and affixed inside a borosilicate glass vial with K_2SiO_3. The specimens were then placed in a transformer steel shielded room in the Paleomagnetic Laboratory at Scripps Institution of Oceanography for the duration of the experiment.

2.2.3 IZZI modified Thellier-Thellier Experiment

We conducted the IZZI-modified Thellier-Thellier protocol (Yu et al., 2004; Tauxe & Staudigel, 2004), whereby specimens are incrementally heated and cooled either in the absence of a magnetic field to demagnetize the NRM (a zero-field step) or in the presence of an applied lab field to impart a pTRM (an in-field step). Specimens were subjected to both an in-field (I) and zero-field (Z) treatment at each temperature step. Temperature steps were conducted at 100°C intervals from 0°C to 400°C, then 25°C intervals to 500°C, and finally at 10°C intervals until each specimen was completely demagnetized. Specimens were heated in custom-built furnaces in the Scripps Paleomagnetic Laboratory; these furnaces have thermocouples in non-inductively wound heating elements to control the temperature to within a few degrees with reproducibility of better than one degree. Specimens were rapidly air-cooled following treatment. During in-field treatment steps, specimens were cooled in fields of various strengths (initially 30 μT). The order of the treatment, IZ (Aitken et al., 1988) or ZI (Coe, 1967), alternated with each temperature step in order to detect tails (pTRMs imparted at a given temperature that were not removed by treatment in zero field at the same temperature), and zero-field memory effects (Aitken et al., 1988) in the ZI sequence. We applied pTRM checks, additional in-field treatments at a previously measured temperature step, between the ZI and the IZ sequences in order to monitor mineral neoformation and magnetomineral alteration (Coe, 1967). Immediately following treatment, we measured the magnetic remanence with a 2G Cryogenic SQUID (superconducting quantum interference device) magnetometer in the Scripps Paleomagnetic Laboratory.

We conducted a preliminary IZZI-modified Thellier Thellier experiment (Yu et al., 2004; Tauxe & Staudigel, 2004) on 144 specimens from 99 samples, with, one to two specimens from each sample. The results from this preliminary experiment allowed us to target our efforts to the most promising sites from which we selected up to six additional specimens. In total, we measured 381 specimens.

2.2.4 Cooling Rate

The TRM acquired by each specimen is affected by its rate of cooling (Dodson & McClelland-Brown, 1980; Halgedahl & Fuller, 1980; Fox & Aitken, 1980; Santos & Tauxe, 2019). After each treatment, specimens were rapidly air-cooled to match the rate at which we suspect these very fine grained specimens initially cooled. To assess the possible impact of cooling rate on TRM acquisition in our specimens compared to those studied by (Lawrence et al., 2009) from the presumably slower cooled lava flow interiors, we conducted a cooling rate experiment whereby we heated the specimens to 620° in a 50 μT field, cooled them as before (in under an hour), and then measured their TRM. We then re-heated the specimens to 620° in a 50 μT field and allowed them to cool without a fan (approximately 12 hours), and remeasured the resulting TRM. The ratio of the two measurements allows us to assess the effect of cooling rate on the TRM.

2.2.5 Non-linear TRM Acquisition

The Thellier method (Thellier & Thellier, 1959) is based on the assumption of single domian (SD) non-interacting grains of magnetite that acquire a TRM in proportion to the ambient field in low magnetic fields, yet several studies have detected non-linear TRM acquisition (e.g., Selkin et al. (2007); Ben-Yosef et al. (2009)). Therefore after we completed the IZZI-experiment, we selected specimens from sites that met the CCRIT criteria in both our and Lawrence et al. (2009)'s experiments. For these, we performed an additional set of steps to detect non-linear TRM acquisition behavior. We subjected these specimens to a total TRM by cooling from 630° C, in treatment fields of 0, 15, 20, 30, 40, 50, and 60 μT.

2.3 Paleodirection

2.3.1 Alternating field demagnetization and thermal demagnetization

Lawrence et al. (2009) recovered paleodirections by stepwise thermal demagnetization or alternating field (AF) demagnetization. Each oriented drill core was cut into one-inch specimens, at least five of which were subjected to either AF or thermal demagnetization. A total of 461 specimens were AF demagnetized in a Sapphire Instruments SI-4 uniaxial AF demagnetizer in the Scripps laboratory. Specimens were treated in 5 mT steps from 5 mT – 20 mT, 10 mT steps from 20 mT – 100 mT, and then at 120 mT, 150 mT, and 180 mT or until the NRM was removed. An additional 323 specimens were thermally demagnetized by stepwise heating in 50°C intervals from 0°C – 500°C, in 25°C intervals from 520°C to 560°C and in 5°C-10°C intervals until the specimens were entirely demagnetized. After each treatment, the remaining NRM was measured. The demagnetization path, as represented by Zijderveld diagrams (Zijderveld, 1967) monitors the stability and behavior of the magnetization vector as the specimen is demagnetized. For this study, we thermally demagnetized an additional 44 specimens to increase the number of paleodirectional estimates per site from 5 to 6 following the suggestion of Behar et al. (2019) who found decreased scatter and increased consistency with GAD by using more specimens per site and stricter within site scatter criteria.

2.4 Hysteresis and FORCs

Lawrence et al. (2009) describe paleointensity experiments on specimens that were drilled from the interior of the lava flows including those collected by Mankinen and Cox (1988) and analyzed by Tauxe et al. (2004). Here we report on new experiments on samples that were hand collected from the surface or base of the lava flow. As described in the following, six sites had specimens with successful intensity estimates from samples collected from both the interior (presumably coarser grained) and the flow top. We selected sister specimens from these sites and measured hysteresis loops and FORC diagrams (Roberts & Verosub, 2000) with a Princeton Measurements Corporation Micromag Alternating Gradient Magnetometer in an attempt to diagnose domain state. We plotted the results using the FORCinel software package (Harrison & Feinberg, 2008).

2.5 ^{40}Ar/^{39}Ar Geochronology

Eighteen samples were selected for ^{40}Ar/^{39}Ar age dating. All Ar-Ar age analyses were conducted at the Argon Geochronology lab at Oregon State University following the procedure of Koppers et al. (2000); Koppers (2003); Koppers et al. (2008). A 200–300 μm groundmass specimen was selected from each sample and then rinsed with distilled water and leached in an ultrasonic bath with HNO_3^- to remove any alteration products. Once cleaned, samples were irradiated in the TRIGA CLICIT nuclear reactor at OSU to convert ^{39}K to ^{39}Ar. The irradiated samples were then incrementally heated in 21-44 temperature steps for 5–7 minutes each. At each temperature step, a defocused CO_2 laser beam scanned the sample to release the Argon. Argon isotopes were then measured by an ARGUS-VI Mass Spectrometer.

At each temperature step, Ar isotopes ^{36}Ar, ^{39}Ar, and ^{40}Ar are measured. The age of the sample is estimated by a heating plateau age and an inverse isochron age that are compared to ensure the two estimates are concordant at the 95% confidence level. To estimate the heating plateau age, an age and uncertainty is first calculated for each temperature step by using the ratio of ^{40}Ar to ^{39}Ar. A plateau is then selected from this age spectrum that includes at least three incremental heating steps with overlapping 2σ confidence levels and at least 50% of the total $39\mathrm{Ar}_k$ released. The heating plateau age of the sample is estimated from the mean plateau age and its reliability by the Mean Square Weighted Deviate (MSWD). To determine the inverse isochron age, the ratio of ^{36}Ar/^{40}Ar is plotted against ^{39}Ar/^{40}Ar. A regression line is selected that includes at least 5 heating steps and each data point to within 3σ of the ^{39}Ar/^{40}Ar and ^{36}Ar/^{40}Ar weighted means (Heaton & Koppers, 2019). The inverse isochron age is calculated with the value of ^{39}Ar/^{40}Ar when ^{36}Ar/^{40}Ar is 0.

3 Results

3.1 Paleointensity

We present the results of our IZZI experiment as Arai diagrams (Nagata et al., 1963), in order to compare the ratio between NRM remaining to pTRM acquired for each pair of temperature steps and to monitor any changes in this ratio. We present the magnetization directions as Zijderveld diagrams (Zijderveld, 1967) and calculate the best fitting direction or plane, through the vectors using principal component analysis (Kirschvink, 1980). Despite our best effort to collect micro-crystalline material, our specimens often did not behave as the non-interacting uniaxial single domain grains of magnetite assumed by Néel theory (Néel, 1955) and required by Thellier's Laws (Thellier & Thellier, 1959). Instead, many specimens exhibit non-ideal behavior (i.e. zig-zagging, failed pTRM checks, or multiple components of magnetization) resulting in potentially unreliable paleointensity estimates.

3.1.1 Non-ideal behavior: Zig-zagging

Zig-zagging in the Arai diagram (Figure 4a,e) occurs when the ratio of NRM remaining to pTRM acquired varies between different temperature intervals based on the sequence of treatment steps (IZ or ZI). During the IZZI modified Thellier-Thellier experiment, the order in which the treatments are applied, in-field then zero-field or zero-field then in-field, alternates at each temperature step (Yu et al., 2004). The alternating sequence is used to detect so-called 'pTRM tails' (Shashkanov & Metallova, 1972) and zero-field memory effects (Aitken et al., 1988). Tails occur either when the pTRM

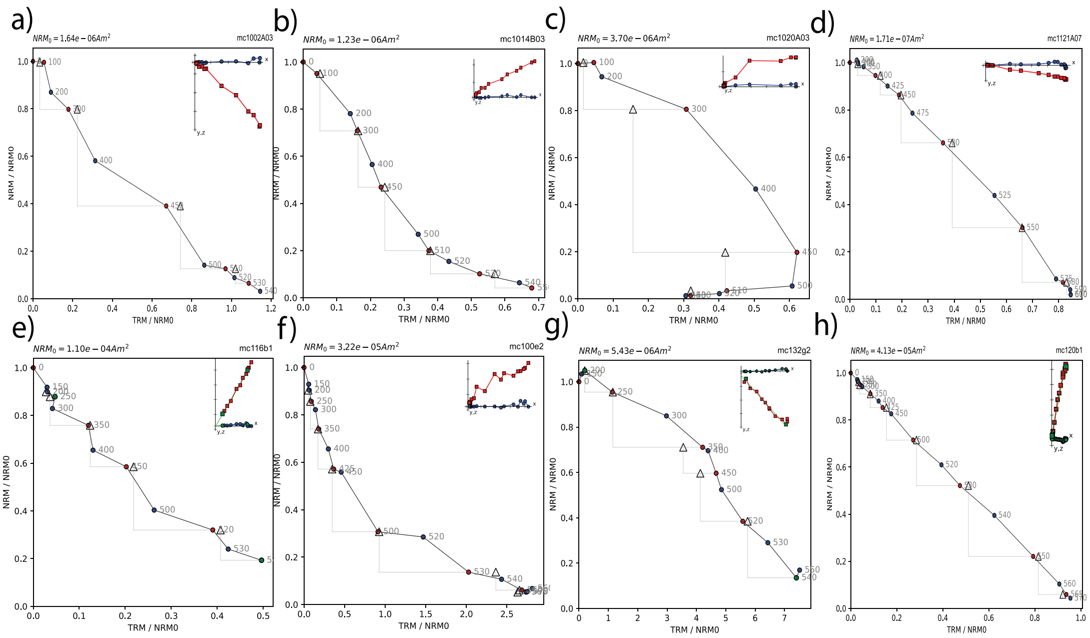

Figure 4. Representative Arai and Zijderveld diagrams (insets) of the different behaviors observed in our unoriented specimens. White triangles mark pTRM checks while circles indicate the sequence of treatments- in-field treatment preceding a zero-field treatment (red circles) or zero-field treatment preceding an in-field treatment (blue circles). a - d) are results from this study and e - f) from (Lawrence et al., 2009). a,e) zig-zagging; b,f) non-linearity and sagging; c,g) failed pTRM checks; d,h) 'well-behaved' specimens where the proportion of NRM remaining to pTRM acquired is identical between each set of temperature steps.

acquired by heating to temperature T in a field is not entirely removed when the specimen is reheated to temperature T and cooled in a zero-field (a high temperature tail) or when the pTRM is removed at a lower temperature (a low temperature tail). This behavior likely indicates the presence of non-SD grains (Dunlop & Özdemir, 2001).

3.1.2 Non-ideal behavior: Failed pTRM checks

A pTRM check, for which a previously measured in-field treatment is repeated, is inserted after every ZI-IZ pair (Coe, 1967; Tauxe & Staudigel, 2004). Any deviation in the remanence (Figure 4b) indicates magneto-mineral alteration or changes in the blocking and unblocking temperature spectra perhaps due to the presence of non-SD grains (Shcherbakov et al., 1993).

3.1.3 Ideal behavior and Selection Criteria

To filter out the specimens that exhibited non-ideal behavior (Figure 4), we applied a set of selection criteria at the specimen and site level. A wide range of selection criteria (Selkin & Tauxe, 2000; Leonhardt et al., 2004; Kissel & Laj, 2004; Tauxe et al., 2016) and paleointensity statistics (Paterson et al., 2014) exists to separate low and high quality paleointensity data. We modeled our criteria (Table 1) after those of Cromwell et al. (2015), in which they successfully recovered accurate and precise estimates of paleointensity of historical Hawaiian lava flows. This set is referred to as the 'CCRIT' set of paleointensity criteria (Tauxe et al., 2016).

n	DANG	MAD	β	SCAT	Frac	G_{max}	$\left\|\vec{k}\right\|$	N	$B_{\%}$	$B\sigma$
4	$\leq 5°$	$\leq 5°$	0.1	TRUE	0.78	$\leq$0.6	0.164	3	10	4 μT

Table 1. Selection criteria (Paterson et al., 2014) applied to the data from the IZZI-modified Thellier-Thellier experiment: n = minimum number of consecutive demagnetization steps, DANG = deviation angle, MAD = maximum angle of deviation, β = the maximum ratio of the standard error to the best fit slope, SCAT = a boolean value that indicates whether the data fall within $2\sigma_{threshold}$ of the best fit slope, FRAC = fractional remanence, G_{max} = maximum fractional remanence removed between consecutive temperature steps, $\overrightarrow{k}$ = maximum curvature statistic (1/radius of the best-fitting circle), N = minimum number of specimens per sample, $B_{\%}$ = maximum percentage standard deviation from the site average intensity, B_{σ} = maximum intensity (μT) deviation from the site average intensity.

CCRIT applies two directional statistics, Deviation ANGle (α of Selkin and Tauxe (2000), *dev* of Tanaka and Kobayashi (2003) and DANG in (Paterson et al., 2014)) and maximum angle of deviation (MAD) (Kirschvink, 1980) to determine the variability in the direction of the NRM. MAD quantifies the amount of scatter in the directions while DANG calculates the angle between the best-fit line for the demagnetization direction and the origin. Three additional parameters are SCAT and FRAC of Shaar and Tauxe (2013), and $|\overrightarrow{k}|$ of Paterson (2011) applied over interval used (k') of (Cromwell et al., 2015); these are applied to test the assumption of linearity of the Arai plot. SCAT constrains the amount of scatter permitted between the best fit proportionality constant and the demagnetization data and pTRM checks; FRAC ensures the majority of the remanence is used to calculate paleointensity; $\overrightarrow{k}$ quantifies the amount of curvature. CCRIT also tests for consistency between estimates at the site level by setting thresholds on the percent error (β_{σ}%) and standard deviation (β_{σ}) permitted for specimen at a site. Twenty-eight of our original 135 sites passed these selection criteria (see Supporting Table S2).

3.2 Paleodirection

The results of the demagnetization experiments vary from multiple unstable directions (e.g., Figure 5a,b,c) to a single stable direction (e.g., Figure 5 d,e). Multiple directions with distinct coercivity and blocking temperature spectra decay along one direction at low field and temperature treatments then abruptly shift to decay along a different direction for the final, characteristic, remanent magnetization (ChRM) (Figure 5a,b). The low temperature or low coercivity component may result from a viscous remanent magnetization or a partial overprint that is typically removed after the first or second treatment. Multiple components with overlapping blocking temperature spectra appear as zig-zagging or gradual shifts in the demagnetization curve (Figure 5c). Zig-zagging may result from tails, if the thermal demagnetization data was derived from an IZZI experiment. We observe gradual changes in the magnetization direction where there may be multiple directional components that are removed in different proportions between each treatment step. We applied a set of criteria (Table 3.2) to select the final stable component of the demagnetization vector, the ChRM. At the specimen level, at least 4 demagnetization steps were used to determine the ChRM and MAD and DANG were set to 5° to constrain the direction. Lawrence et al. (2009) used site level thresholds of $N > 4$ and $\kappa > 50$ as acceptance criteria. To ensure consistent directions within a site, we required at least 6 samples per site (N) to calculate the site average direction and set the minimum threshold for κ (Fisher, 1953), a precision parameter to quantify the dispersion in the directions, to 100. One-hundred and eleven sites yield reliable paleodirections (Table 4).

MAD	DANG	N	k
$\leq 5\,^\circ$	$\leq 5\,^\circ$	≥ 6	≥ 100

Table 2. Selection criteria applied to our directional data: MAD = maximum angle of deviation, DANG = deviation angle, N = minimum cores per site, k = precision parameter

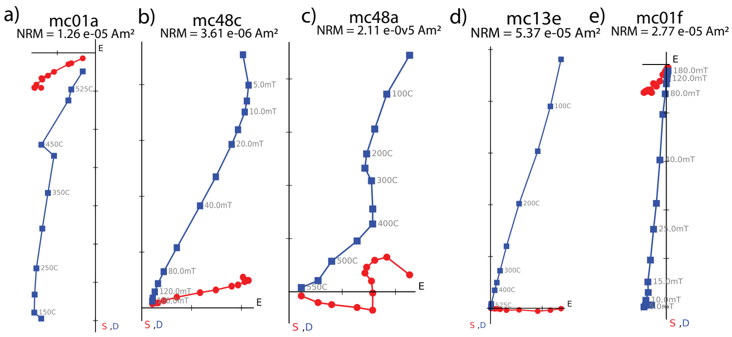

Figure 5. Representative Zijderveld diagrams of the directional behaviors observed in our specimens. The projection of the demagnetization vector onto the vertical plane is marked in blue and the projection of the same vector onto the horizontal plane is marked in red. a) Two reverse directions with distinct blocking temperature spectra. A low temperature direction is removed 0 – 300 ° and a higher temperature component demagnetizes between 400 °-600 °. b) Two normal directions with distinct coercivity spetra. The low coercivity component is removed between 0 - 10 mT. c) An unstable normal direction from a thermal demagnetization experiment. The specimen may include several directions with overlapping blocking temperature spectra. d) A single stable normal direction from a thermal demagnetization experiment e) A single stable reverse direction from an AF demagnetization experiment.

3.3 Hysteresis and FORCs

Several sites (mc1030, mc1032, mc1115, mc11121, mc1147, and mc1157) passed CCRIT and included estimates from samples that were collected from both the interior (Lawrence et al., 2009) and surface of the same lava flow (this study). At sites mc1030, mc1115, mc1147, and mc1157, the estimates from the interior are $2\mu T$ - $8\mu T$ lower than the paleointensity estimates from the lava flow tops (Figure 6). We selected sister specimen for hysteresis loops and FORCs (Harrison & Feinberg, 2008) to examine the domain state or magnetic interactions that may explain the difference.

Although each sister specimen passed CCRIT, the specimens exhibit a mixture of magnetic components in the FORCs. We interpret the horizontal ridge in the FORC diagram near $B_u = 0$ mT (Figure 7) as the contribution from single domain grains after Roberts and Verosub (2000) and Pike et al. (2001). The distribution of coercivities (B_c) ranges from 0 to 50 mT and peaks between 0 and 20 mT. This peak is offset from

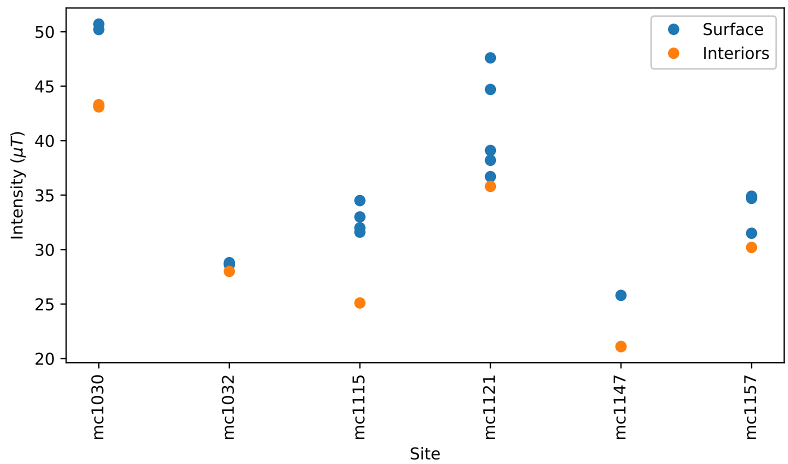

Figure 6. Paleointensity estimates from sites that pass CCRIT and include data from both the lava flow top (blue circles) and the lava flow interior (orange circles).

the $B_u = 0$ mT axis. The contours are shifted downward from this ridge, which reflects the level of interaction fields between the single domain grains. Each specimen displays superparamagnetic behavior as inferred from the vertical ridge near $B_c = 0$ mT that peaks around $B_u = 0$ mT.

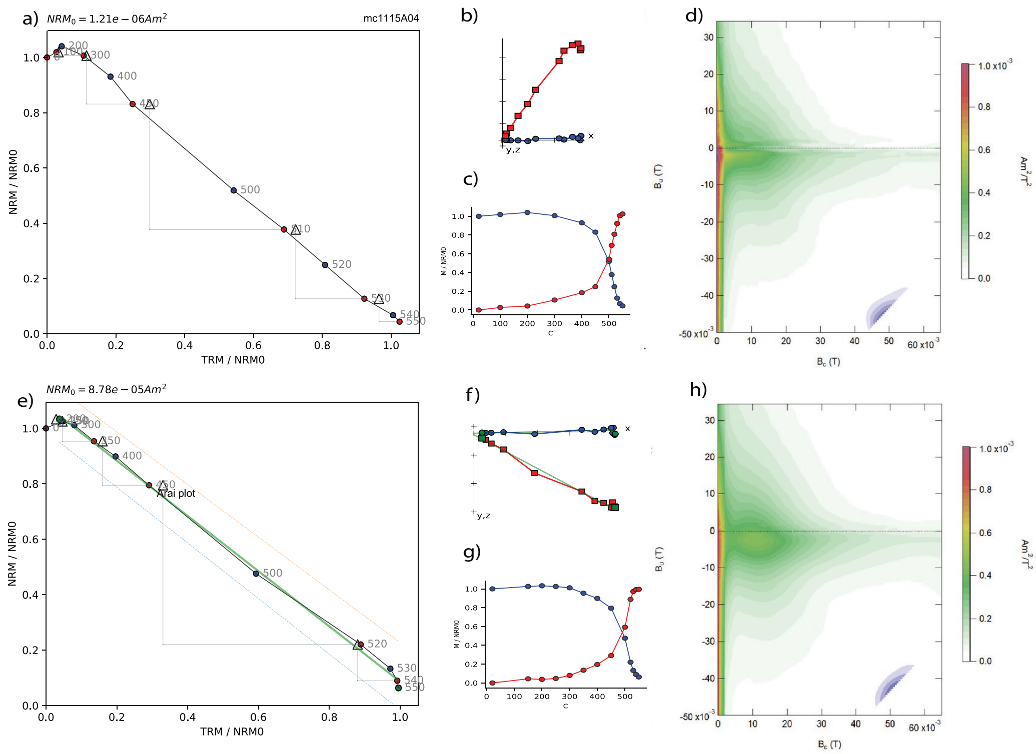

Figure 7. Arai diagram (a,e), Zijderveld diagram (b, f), MT curve (c,g), and FORC diagrams (d,h) for samples from site mc1115 that passed CCRIT. Specimen mc115A04 (a -d) was sampled from the lava flow top and yielded a 31.55 μT paleointensity while mc115a2 (e-h) was collected from the lava flow interior and estimated a 25.15 μT paleointensity

3.4 ^{40}Ar/^{39}Ar Geochronology

We present thirteen new ^{40}Ar/^{39}Ar age analysis from the Erebus Volcanic Province (see supporting information Table S2). Site ages were determined by their plateau age. Each plateau age estimate includes over 60% of the $^{39}Ar_k$ released, excluding sites mc1034, mc1131, and mc1157 which only include 52%, 50%, and 44% of the $^{39}Ar_k$ released, respectively (Figure 8). Samples give plateau ages that are concordant with their inverse isochron ages. Two samples from site mc1033 yield significantly different age estimates, so we exclude both.

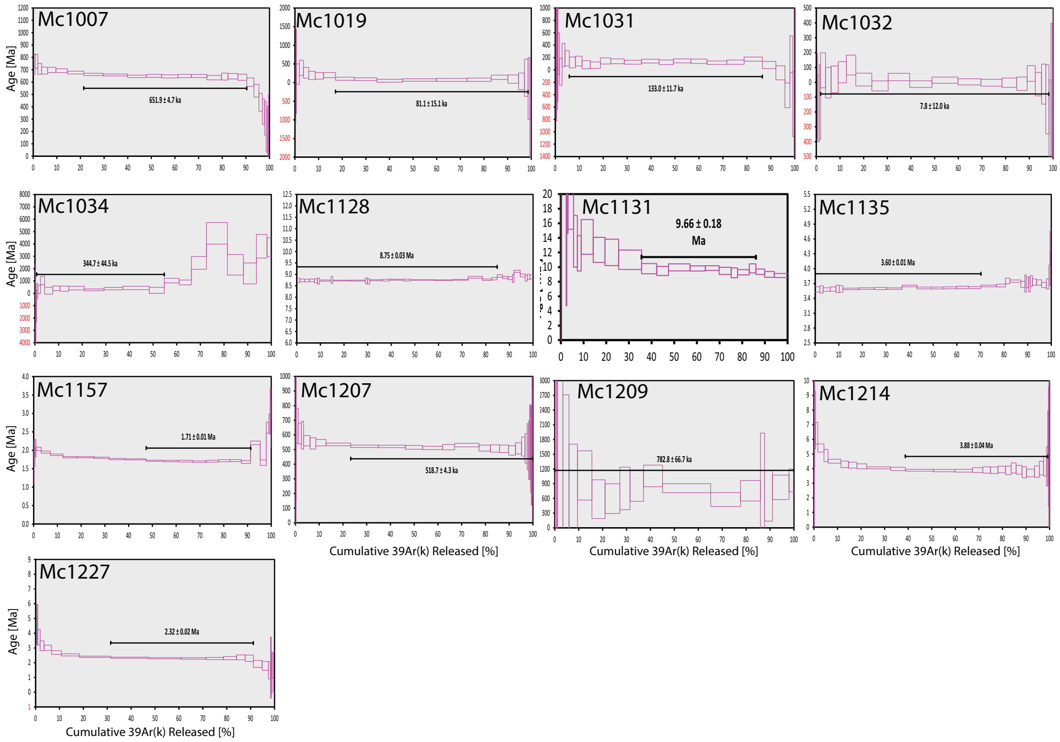

Figure 8. Results from the ^{40}Ar/^{39} incremental heating method used to date 13 sites. Black bars mark the bounds of the age spectra plateau that were used to estimate the site age.

4 Discussion

4.1 Examining the GAD structure of the ancient magnetic field

4.1.1 Paleointensities

Our new paleointensity dataset consists of 28 sites that pass CCRIT. We converted the paleointensities to their corresponding virtual axial dipole moments (VADMs) to compare intensity estimates across latitudes (Table 3). VADM is the strength of the axial dipole moment that would generate the intensity observed at a given latitude. Our 28 sites yield a median intensity of 33.01 μT $\pm$ 2.59 μT or equivalently a median paleomagnetic axial dipole moment (PADM) of 43.40 ZAm$^2\pm$ 3.41 ZAm^2. Our median intensity estimate is slightly higher than that of Lawrence et al. (2009) and about half of the modern intensity measured in the Erebus Volcanic Province ($\sim$62 μT). This is consistent with predictions of an average dipole moment of $\sim$42-50 Am^2 (e.g., Juarez et al. (1998); Selkin and Tauxe (2000); Tauxe et al. (2013); Wang et al. (2015)) over the long term. However, there remains the problem that the data from the last few million years from the global dataset show no dependence of field strength on latitude (Figure 2) which, if true, belies the existence of a single geocentric axial dipole moment sampled by all the studies.

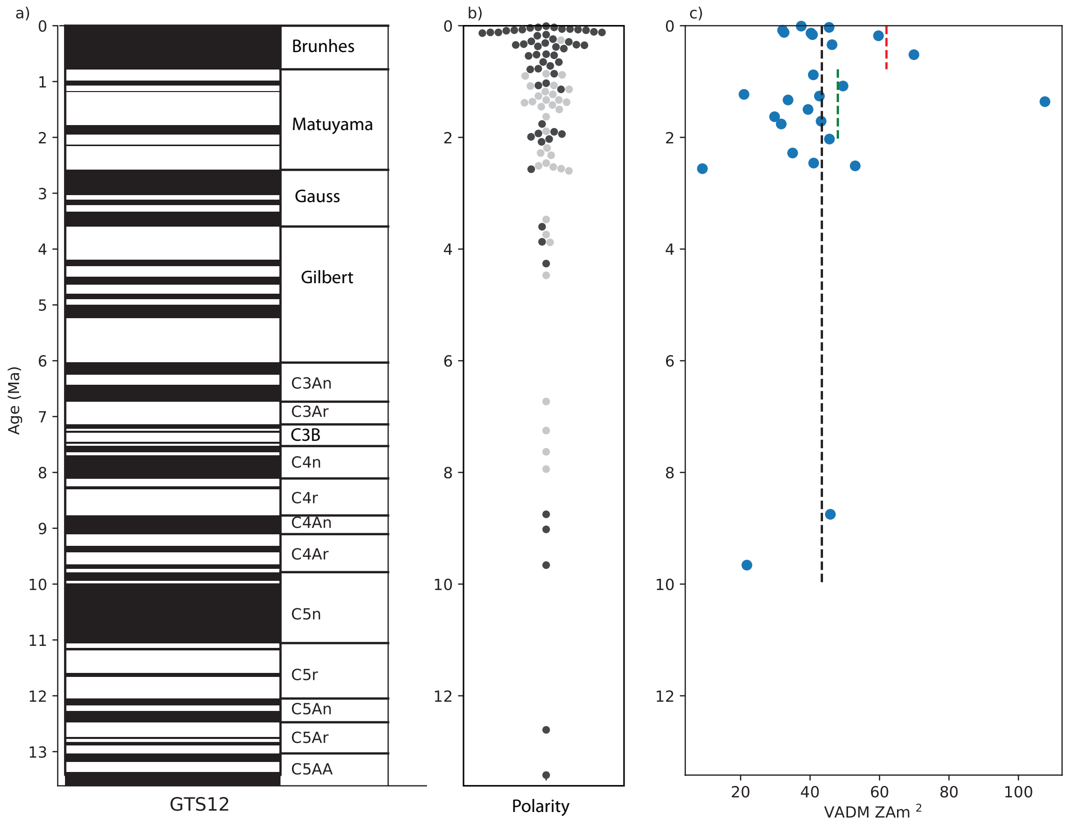

Figure 9. a) The 2012 Geomagnetic Polarity Timescale for the Late Neogene (Gradstein et al., 2012). b) The distribution of ages for our sites, colored by normal (black) and reverse (white) polarity. c) The distribution of VADM computed in this study. Red (green) dashed lines are PADMs from Zeigler et al. (2011) for the Brunhes and Matuyama (<2 Ma) respectively. Dashed black line is the average PADM for this study.

To assess the structure of the paleomagnetic field over the Late Neogene, we compare our results to globally distributed paleointensity data stored in the PINT database of Biggin et al. (2009). While our estimated PADM of 43.40 ZAm^2± 3.41 ZAm^2 is consistent with many recent estimates for the long term average (e.g., (Juarez et al., 1998; Selkin & Tauxe, 2000; Ziegler et al., 2011; Tauxe et al., 2013; Wang et al., 2015)), our intensity estimate at the high southerly latitudes, when compared to the global data set, does not display the latitudinal dependence of intensity expected of a GAD generated field (Figure 2) and appears depressed when compared to the global paleointensity dataset over the Late Neogene.

The apparent discrepancy between our results and the global dataset could result from a PADM of ∼45 ZAm^2, which is substantially weaker than the modern dipole moment of ∼77 ZAm^2. However, we would expect to recover even lower intensities at lower latitude sites (∼15 μT at the equator) from this weaker dipole. Although a few recent studies (Wang et al., 2015) have published results in agreement with this prediction, many older studies from mid and low latitudes have much higher values (Figure 2) than predicted by a PADM of $\sim 40 - 50$ ZAm2.

The reasons for the lack of a dipole signal in the global dataset are not clear. The results from some experimental protocols may be biased (e.g., Cromwell, Trusdell, et al.

Site	Lat(°)	Lon (°)	VADM (ZAm^2)	n	Intensity (μT)	Age (Ma)
mc1004	-77.84	166.69	46.33	3	35.23	0.34 ± 0.01
mc1015	-77.46	169.21	33.66	3	25.57	1.33 ± 0.02
mc1019	-77.88	165.30	32.08	3	24.40	0.0811 ± 0.0151
mc1029	-78.31	164.79	59.70	7	45.46	0.18 ± 0.08
mc1030	-78.34	164.88	61.49	4	46.82	
mc1031	-78.35	164.30	40.27	3	30.67	0.133 ± 0.0117
mc1032	-78.35	164.30	37.46	4	28.52	0.0078 ± 0.012
mc1035	-78.39	164.24	32.52	3	24.77	0.12 ± 0.02
mc1109	-78.28	163.54	42.69	3	32.50	1.26 ± 0.04
mc1115	-78.24	162.96	41.04	5	31.24	2.46 ± 0.31
mc1117	-78.24	162.97	34.98	4	26.62	2.28 ± 0.24
mc1119	-78.24	162.96	49.49	4	37.67	1.08 ± 0.22
mc1120	-78.24	163.09	31.70	3	24.13	1.76 ± 0.05
mc1121	-78.23	162.95	53.00	6	40.35	2.51 ± 0.06
mc1128	-78.21	166.57	45.85	3	34.90	8.75 ± 0.03
mc1131	-78.21	166.57	21.81	5	16.60	9.66 ± 0.18
mc1139	-78.26	163.08	40.94	3	31.17	0.88 ± 0.08
mc1140	-78.28	163.00	45.58	3	34.70	2.03 ± 0.09
mc1142	-77.85	166.68	20.98	4	15.95	1.23 ± 0.02
mc1147	-78.20	162.96	29.78	3	22.67	1.63 ± 0.34
mc1155	-77.70	162.25	39.42	3	29.97	1.5 ± 0.05
mc1157	-77.70	162.26	43.18	4	32.83	1.71 ± 0.01
mc1164	-77.51	169.33	107.63	3	81.77	1.36 ± 0.01
mc1167	-77.49	169.29	58.49	3	44.43	
mc1207	-77.68	166.52	69.91	3	53.13	0.5187 ± 0.0043
mc1217	-77.51	167.44	40.70	5	30.92	0.16 ± 0.01
mc1218	-77.56	166.98	45.48	5	34.56	0.03 ± 0.01
mc1306	-77.70	162.69	9.00	3	6.84	2.56 ± 0.13

Table 3. Successful paleointensity results from this study. VADM: virtual axial dipole moment (ZAm^2), Intensity: paleointensity (μT), n: samples.

(2018); Cai et al. (2017)). Bias in temporal sampling toward the present could also cause a high bias in the median intensity as more recent data appear to have higher intensities (Selkin & Tauxe, 2000; Ziegler et al., 2011). Sampling material may also affect paleointensity estimates. (Selkin & Tauxe, 2000) recovered the expected latitudinal dependence of paleointensity, with a PADM of ~45 ZAm^2, by examining paleointensties solely from submarine basalt glass. Therefore, in the following section we explore the effect of sampling material on the resulting paleointensity estimate.

4.2 Examining the role of sampling material

In Figure 10 we compare results from our sites that passed CCRIT with the original interpretations of Lawrence et al. (2009). A few sites (mc1147, mc1155, and mc1035) yield similar intensity estimates while others vary by 2 - 15 μT. Six of the original sites have specimens that passed CCRIT and include specimens from both the interior and the surface of the same lava flow. We assume that a single lava flow cooled quasi-instantaneously, so the surface and interior of the flow should preserve identical intensities. However, at these sites (Figure 6), specimens from the interior yield systematically lower paleointensities than those from the flow top by 2 μT - 8 μT.

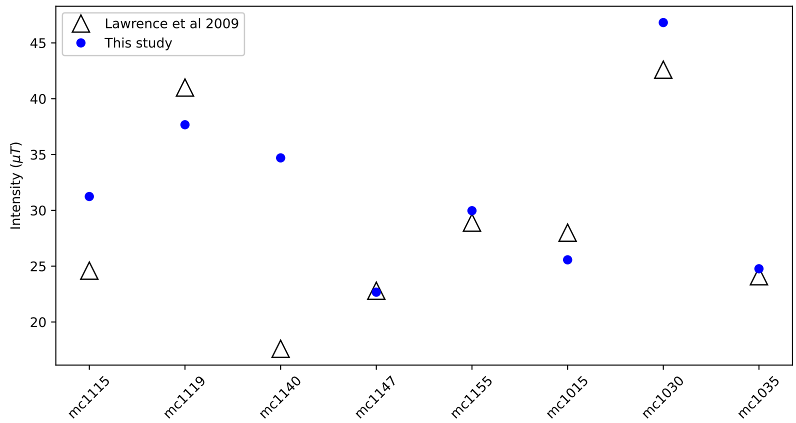

Figure 10. Average intensity estimates for the sites in this study that passed CCRIT (blue dots) and the sites from Lawrence et al. 2009 (white triangles) that passed their set of selection criteria.

A slower cooling rate may result in a higher intensity of magnetizationDodson and McClelland-Brown (1980); Santos and Tauxe (2019)) so we tested the effect of cooling rate on the TRM of the specimens by conducting a cooling rate experiment. Each specimen preserved a higher remanence following slow cooling than fast cooling as expected from SD theory (see supporting information Figure S5). Therefore differences in the cooling history between the two sampling regions (i.e that the flow tops cooled more quickly than the flow interiors) does not explain the lower paleointensities we measure in the interior, if they are both single domain.

Next, we tested whether differences in domain state or magnetic interaction could explain the behavior by measuring hysteresis loops and FORC diagrams (Pike et al., 1999). The magnetic moments in specimens from mc1115 (Figure 7) and mc1147 (see supporting information Figure S6) include a superparamagnetic component, a single domain component and some degree of interaction (Roberts & Verosub, 2000), but the domain structure of specimens from the interiors appears broadly similar to those from the flow tops at the same site for the specimens that passed CCRIT tested here. Therefore, differences in domain states do not account for the higher paleointensities measured in the samples collected from the surface.

In addition to cooling rate and domain state, we investigated whether non-linear TRM acquisition could explain the bias in the intensity estimates from the interior. Our samples, collected from the surface during the 2016/2017 field season, were treated in a 30 μT field during the in-field steps of the IZZI experiment. Lawrence et al. (2009) cooled some specimens from the interior in a 25 μT field and other specimens in a 30 μT field. To test for non-linearity, we performed TRM acquisition tests in fields from 0 to 60 μT to investigate whether the lower intensities measured in the interiors resulted from the lower intensities applied during the IZZI experiment (Supporting information Figure S7). All specimens showed linear behavior with applied field. Thus, neither cooling rate, domain state, nor non-linear TRM acquisition accounts for the lower intensities recorded by the specimens sampled from the interior of the lava flows. Only six of our 28 successful sites include paleointensity estimates from both the surface and the interior. We believe the intensity estimates that pass CCRIT from both contexts preserve reliable intensity estimates. A full investigation on the role of sampling material on paleointensity estimates would require a larger sample size.

4.2.1 Paleodirections

4.2.1.1 Paleopole We have compiled our new directional data with the data of Lawrence et al. (2009) (see supporting Table S1 for combined sites) and (re)analyzed all of the directional data. Our new dataset consists of 107 site-mean directions that pass our (stricter) selection criteria (Table 4). It includes 66 normal polarity (Figure 11a) and 41 reverse polarity (Figure 11b) site-mean directions (Table 5). We applied a bootstrap reversal test (Tauxe et al., 1991) on the reverse and normal directions. The directions pass the reversal test, so the two sets are indistinguishable (see supporting information Figure S2) and we can combine the antipodes of the reverse directions with the normal directions and analyze the combined dataset.

Site	k	N	Dec (°)	Inc (°)	α_{95} (°)	VGP Lat (°)	VGP Lon (°)	Lat (°)	Lon (°)	Age (Ma)
mc1001	356	6	255.3	79.7	3.55	69.49	275.43	-77.85	166.64	1.18 ± 0.01
mc1002	290	6	334.4	-79.1	3.93	78.61	114.74	-77.85	166.69	0.33 ± 0.02
mc1008	361	8	39.4	-77.6	2.92	73.85	233.48	-77.80	166.83	0.65 ± 0.05
mc1009	192	8	253.8	-82.8	4.00	68.81	26.53	-77.55	166.20	0.07 ± 0.02
mc1010	217	7	335.9	-77.6	4.11	76.61	120.83	-77.57	166.23	
mc1011	452	8	325.2	-76.8	2.61	73.59	107.24	-77.57	166.23	
mc1014	450	8	0.5	-80.6	2.61	84.16	170.66	-77.46	169.23	
mc1015	949	9	172.2	84.6	1.67	87.61	26.42	-77.47	169.23	1.33 ± 0.02
mc1020	128	7	137.9	-79.3	5.34	59.24	317.40	-77.88	165.02	0.77 ± 0.032
mc1021	301	8	333.1	80.5	3.20	60.56	329.58	-78.21	166.49	
mc1029	106	6	25.2	-78.5	6.52	77.47	212.51	-78.31	164.80	0.18 ± 0.08
mc1030	140	8	242.5	68.8	4.69	56.23	242.70	-78.34	164.87	
mc1032	168	7	266.1	-75.3	4.66	59.48	49.92	-78.36	164.30	0.0078 ± 0.012
mc1033	381	8	9.6	-74.5	2.84	72.39	179.81	-78.38	164.34	
mc1034	393	7	281.6	-82.2	3.05	72.85	45.41	-78.39	164.27	0.3447 ± 0.0445
mc1035	316	8	301.6	-84.7	3.12	79.22	40.38	-78.39	164.23	0.12 ± 0.02
mc1036	171	7	348.7	-82.2	4.63	85.40	123.78	-78.39	164.27	0.12 ± 0.02
mc1037	316	8	215.6	81.6	3.12	80.27	242.85	-78.40	164.27	4.47 ± 0.04
mc1038	227	7	295.7	-77.9	4.02	69.23	71.27	-78.40	164.21	
mc1039	371	7	282.7	-87.3	3.14	78.34	11.16	-78.39	164.21	0.08 ± 0.01
mc1040	215	7	194.4	-83.0	4.12	64.85	352.17	-78.39	164.20	
mc1041	144	6	270.5	-78.3	5.59	64.85	48.78	-78.39	164.20	0.28 ± 0.02
mc1043	104	6	280.5	-85.1	6.57	76.31	28.83	-78.37	164.24	
mc1044	161	8	325.2	-74.1	4.37	68.86	112.55	-78.36	164.26	
mc1048	229	6	75.8	-54.9	4.43	37.46	247.79	-78.24	163.36	
mc1100	163	6	12.6	-74.3	5.26	71.94	182.97	-78.30	162.90	0.86 ± 0.23
mc1101	863	6	35.8	-79.1	2.28	76.69	228.48	-78.31	162.93	1.07 ± 0.01
mc1103	220	7	136.7	71.2	4.07	63.25	104.41	-78.24	163.36	1.42 ± 0.03
mc1104	236	6	69.0	-75.5	4.37	64.56	256.04	-78.24	163.40	0.29 ± 0.02
mc1106	434	6	18.4	-76.3	3.22	74.72	194.98	-78.21	163.31	13.42 ± 0.18
mc1107	783	6	95.5	-84.5	2.40	73.27	302.68	-78.20	163.35	2.57 ± 0.38
mc1109	661	6	172.6	76.0	2.61	74.98	150.65	-78.28	163.54	1.26 ± 0.04
mc1110	245	6	253.4	80.0	4.28	70.49	270.66	-78.24	163.44	7.94 ± 0.24
mc1111	1193	7	47.9	-67.8	1.75	57.63	224.04	-78.22	162.79	1.99 ± 0.04
mc1112	159	6	232.9	74.4	5.31	66.17	237.62	-78.24	163.44	7.63 ± 0.32
mc1113	130	7	257.0	77.6	5.30	66.13	266.80	-78.23	162.74	6.73 ± 0.17
mc1115	222	6	74.9	67.5	4.50	46.10	45.51	-78.24	162.96	2.46 ± 0.31
mc1116	157	6	275.6	-80.7	5.36	69.44	44.86	-78.22	162.74	1.14 ± 0.11
mc1117	1152	6	169.0	68.9	1.97	63.85	147.72	-78.24	162.97	2.28 ± 0.24
mc1118	108	7	58.6	-52.2	5.82	38.27	229.23	-78.24	163.14	0.31 ± 0.04
mc1119	966	6	126.3	48.4	2.16	35.80	102.92	-78.24	162.96	1.08 ± 0.22

Continued on next page

Site	k	N	Dec (°)	Inc (°)	α_{95} (°)	VGP Lat (°)	VGP Lon (°)	Lat (°)	Lon (°)	Age (Ma)
mc1120	624	9	72.4	-70.5	2.06	56.59	252.58	-78.24	163.09	1.76 ± 0.05
mc1121	641	10	117.8	79.1	1.91	71.47	68.16	-78.24	162.95	2.51 ± 0.06
mc1123	296	8	75.8	-82.5	3.22	73.59	282.42	-78.25	163.73	1.93 ± 0.05
mc1124	385	6	15.2	-72.7	3.42	69.26	186.58	-78.19	163.57	12.61 ± 0.11
mc1125	153	7	342.6	-63.7	4.89	56.39	141.47	-78.25	163.73	4.26 ± 0.18
mc1126	305	7	12.7	-77.9	3.46	77.99	188.33	-78.25	163.74	
mc1127	689	8	325.3	-66.9	2.11	58.62	118.62	-78.25	163.73	1.94 ± 0.07
mc1128	370	8	33.4	-80.8	2.88	79.67	237.79	-78.21	166.57	8.75 ± 0.03
mc1130	257	6	150.1	46.3	4.18	37.66	132.63	-78.21	166.58	7.25 ± 0.07
mc1131	398	8	20.8	-58.6	2.78	50.15	192.03	-78.21	166.57	9.66 ± 0.18
mc1133	305	6	38.8	-85.6	3.84	82.63	298.22	-78.20	166.58	
mc1134	1049	6	11.8	-84.2	2.07	87.60	267.63	-78.22	166.61	9.02 ± 0.05
mc1135	209	8	266.3	-77.6	3.83	62.95	48.78	-78.23	166.56	3.6 ± 0.01
mc1139	892	6	169.8	79.0	2.24	80.05	141.19	-78.26	163.08	0.88 ± 0.08
mc1140	553	6	343.7	-78.7	2.85	79.03	129.91	-78.28	163.00	2.03 ± 0.09
mc1141	100	6	91.4	83.4	6.71	72.36	150.00	-77.58	-77.58	1.31 ± 0.02
mc1142	355	9	318.5	85.3	2.73	69.82	328.38	-77.85	166.68	1.23 ± 0.02
mc1143	188	6	29.8	-52.1	4.90	42.70	197.51	-78.24	162.88	2.08 ± 0.65
mc1144	108	7	198.4	79.6	5.83	80.63	208.42	-77.85	166.69	
mc1145	773	6	27.6	2.6	2.41	9.12	190.86	-78.24	162.89	1.9 ± 0.12
mc1146	122	7	236.1	63.2	5.48	50.34	230.48	-78.22	162.96	1.37 ± 0.42
mc1147	361	6	220.3	64.3	3.53	54.44	213.47	-78.20	162.96	1.63 ± 0.34
mc1148	104	6	283.6	-79.6	6.58	69.09	56.82	-77.49	167.25	0.72 ± 0.66
mc1152	887	6	333.2	-85.6	2.25	84.02	23.24	-77.72	162.65	3.87 ± 0.15
mc1153	161	6	311.2	57.9	5.29	29.98	299.36	-77.76	162.14	2.53 ± 0.13
mc1154	514	6	283.1	87.7	2.96	75.98	324.02	-77.72	162.63	2.19 ± 0.08
mc1155	212	8	230.1	78.1	3.81	72.47	243.37	-77.70	162.25	1.5 ± 0.05
mc1156	381	6	162.7	72.7	3.43	69.56	135.88	-77.70	162.59	1.89 ± 0.13
mc1158	971	6	48.6	43.7	2.15	17.07	27.60	-77.69	162.46	3.74 ± 0.25
mc1160	214	8	233.5	77.8	3.79	71.23	245.95	-77.69	162.35	3.47 ± 0.05
mc1164	1255	7	201.6	85.6	1.70	84.59	312.77	-77.51	169.33	1.36 ± 0.01
mc1165	151	6	159.2	79.6	5.45	80.45	121.68	-77.51	169.33	1.45 ± 0.06
mc1167	6080	8	186.2	72.5	0.71	70.11	179.11	-77.49	169.29	
mc1168	197	7	183.7	67.7	4.30	63.16	174.45	-77.49	169.29	1.38 ± 0.05
mc1170	1621	6	2.2	-87.5	1.66	82.76	345.19	-77.85	166.71	1.03 ± 0.1
mc1200	342	6	301.9	-84.8	3.62	78.81	38.42	-77.55	166.16	0.07 ± 0.01
mc1201	347	6	257.4	-79.7	3.60	64.35	36.72	-77.56	166.22	0.09 ± 0.01
mc1202	3487	6	341.2	-46.6	1.13	39.48	144.75	-77.66	166.36	0.54 ± 0.01
mc1205	579	9	283.4	-34.2	2.14	21.20	85.69	-77.66	166.73	0.37 ± 0.02
mc1206	147	9	326.2	-32.6	4.26	27.79	129.99	-77.67	166.78	
mc1207	334	6	46.0	-71.2	3.67	62.99	229.63	-77.68	166.52	0.5187 ± 0.0043
mc1208	256	6	38.3	-66.2	4.19	57.45	216.21	-77.67	166.53	
mc1209	473	6	59.2	-62.7	3.08	49.29	237.50	-77.69	166.37	0.7828 ± 0.0667
mc1210	1141	6	51.6	-69.4	1.98	59.36	233.89	-77.69	166.37	
mc1211	617	8	4.8	-55.5	2.23	48.36	172.17	-77.66	166.34	
mc1214	1575	10	176.2	77.8	1.22	79.35	158.17	-77.22	166.43	3.88 ± 0.04
mc1215	268	8	347.8	-82.4	3.38	86.26	110.24	-77.48	166.89	0.34 ± 0.02
mc1217	114	10	287.0	-71.9	4.54	58.43	74.76	-77.51	167.44	0.16 ± 0.01
mc1218	132	6	343.4	-81.5	5.84	84.10	114.26	-77.56	166.98	0.03 ± 0.01
mc1220	391	10	36.8	-82.4	2.44	81.15	260.37	-77.46	166.91	0.53 ± 0.04
mc1221	454	6	274.1	-82.9	3.15	72.06	37.94	-77.52	166.80	0.12 ± 0.01
mc1222	307	6	190.4	-52.1	3.83	20.45	356.14	-77.54	166.85	0.11 ± 0.01

Continued on next page

Site	k	N	Dec (°)	Inc (°)	α_{95} (°)	VGP Lat (°)	VGP Lon (°)	Lat (°)	Lon (°)	Age (Ma)
mc1223	161	9	59.8	-82.6	4.06	76.53	277.72	-77.66	166.79	0.38 ± 0.03
mc1224	568	6	192.0	-61.0	2.81	29.86	357.10	-77.53	166.88	0.03 ± 0.01
mc1225	1052	6	113.8	-74.6	2.07	54.46	297.40	-77.58	166.80	0.06 ± 0.01
mc1226	1468	6	19.3	-50.6	1.75	42.93	189.46	-77.61	166.77	0.24 ± 0.02
mc1227	2347	6	221.2	61.8	1.38	51.92	218.00	-77.27	166.73	2.32 ± 0.02
mc1228	161	10	212.2	67.7	3.81	60.68	210.15	-77.27	166.38	
mc1229	339	8	99.5	73.1	3.01	58.57	65.93	-77.48	167.15	1.07 ± 0.18
mc1301	707	6	134.2	77.4	2.52	72.13	209.25	-78.22	-78.22	
mc1302	368	11	102.5	-73.9	2.38	55.68	41.92	-78.19	-78.19	0.04 ± 0.01
mc1303	263	17	17.8	-55.1	2.20	47.33	303.94	-77.58	-77.58	1.31 ± 0.02
mc1304	198	13	156.5	75.6	2.95	73.03	243.19	-78.24	-78.24	0.29 ± 0.02
mc1305	482	16	191.3	71.1	1.68	67.07	298.26	-78.24	-78.24	0.9 ± 0.1
mc1306	175	12	171.4	57.1	3.28	49.81	271.69	-77.70	-77.70	2.56 ± 0.13
mc1307	367	18	226.1	75.5	1.81	69.34	351.67	-77.85	-77.85	1.33 ± 0.12

Table 4: Successful paleodirection results: κ: precision parameter, N: cores per site, Dec: declination (°), Inc: inclination (°), α_{95}: Circle of 95% conficence, VGP Lat: virtual geomagnetic pole latitude (°), VGP Lon: virtual geomagnetic pole longitude (°), Lat: site latitude, Lon: site longitude, Age = age (Ma). Site names were modified for this study. Sites from Mankinen and Cox (1988) (mc1-50) are renamed mc1001-mc1050 while those from Lawrence et al. (2009) (mc100-mc229) are renamed mc1100-mc1229. Sites that were recombined for this study are labeled mc1301-mc1307.

A VGP is the coordinates of the geocentric magnetic dipole that would generate the direction measured at a particular location. The paleomagnetic site-mean directions were transformed to their corresponding virtual geomagnetic poles (VGPs) (Figure 11d-f). We calculated the paleomagnetic pole and α_{95} (Fisher, 1953) by taking the average of the VGPs for the normal polarity sites in Figure 11d (176.8°, 87.5°, and α_{95} 6.8°), the antipode of the reverse polarity sites in Figure 11e, (232.7°, 85.6°, and α_{95} 9.5°) and for the combined dataset in Figure 11f (205.6°, 87.1°, and α_{95} 5.5°), see Table 5. The 95% confidence bounds of each paleopole includes the spin axis, so the paleodirections from our study are consistent with a GAD field.

Polarity	N	Dec (°)	Inc (°)	VGP lon (°)	VGP lat (°)	α_{95} (°)
Normal Intervals	66	4.6	-81.1	176.8	87.5	6.8
Reverse Intervals	41	179.2	82.0	232.7	85.6	9.5
Combined	107	2.7	-81.5	205.6	87.1	5.5

Table 5. Paleodirectional results from this study. N: number of sites, Dec: declination, Inc: inclination, VGP lon: VGP longitude, VGP lat: VGP latitude, α_{95}: 95% confidence bounds.

4.2.1.2 VGP Dispersion In addition to testing the GAD hypothesis by comparing the paleopole from this study with the coordinates of the spin axis, we can test the variability of the geomagnetic field, paleosecular variation (PSV), over the Late Neogene by calculating the dispersion of the VGPs about the geographic pole (McElhinny, 1973). VGP dispersion quantifies the scatter in the site-level VGP estimates. The scatter within each site will vary based on the directions selected to calculate the VGP. At the site-level, we follow Behar et al. (2019) in setting the number of cores per site (N) to ≥ 6 and the precision parameter (k) to ≥ 100 as our criteria to minimize VGP dispersion without discarding too many sites, N, that fail to meet these criteria (Table 4). Although the within-

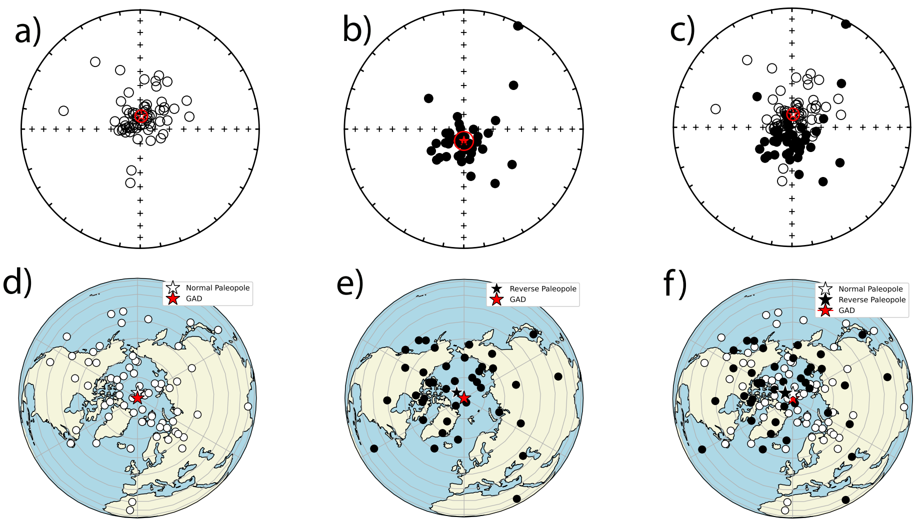

Figure 11. a-c) Equal area projections of the site mean directions that passed our selection criteria along with their corresponding α_{95}s (red circles). Upward (lower) hemisphere projections are open (closed) circles. a) normal polarity directions b) reverse polarity directions and c) all directions. d-e) Maps of the VGPs (circles). The paleopole for each interval is marked with a white star and the GAD as a red star. The α_{95}s around the paleopoles are marked as red circles. d) the normal interval (directions in a), e) the reverse interval (directions in b), and f) the entire dataset (directions in c); the reverse data (black circles) are flipped to the antipode.

site scatter differs between sites, we assume that the N and k cut-offs account for this variability, and so we quantify VGP dispersion using S (Cox, 1970):

$$S^2 = (N-1)^{-1} \sum_{i=1}^{N} (\Delta_i)^2 \tag{5}$$

where N is the number of sites and Δ_i is the angular deviation between the i^{th} VGP and the spin axis. We calculate S_p for the normal poles, the reverse poles, and the combined dataset which includes the antipode of the reverse poles and the normal poles that passed our set of selection criteria (Table 6). We also calculate the 95% bootstrap upper and lower confidence bounds for the VGP dispersion of each dataset. The VGP dispersion is higher for the normal poles than the reverse poles but both results fall within the overlapping 95% bootstrap confidence bounds of the two datasets so the difference in VGP dispersion is insignificant.

For S_{45}, we filter the VGPs that passed our selection criteria by applying a strict 45° VGP cut-off. The rationale for applying cutoffs is that VGPS with low latitudes may reflect directions acquired during transitional or excursional field states. These directions record an unstable geomagnetic field state so VGP cut-offs were introduced to exclude these from the calculation of dispersion (Watkins, 1973). Applying a 45° VGP cut-off, reduces dispersion by $5-8°$. The VGP dispersion is higher in the reverse poles than the normal poles, but once again the poles fall within their overlapping 95% bootstrap confidence bounds so the difference is not significant. Although a VGP cut-off may remove transitional/excursional field directions, it may also underestimate dispersion by excluding'normal' secular variation. For example, a strict 45° VGP cut-off would bias against paleodirections recovered from high latitudes because there is a latitudinal dependence of dispersion- higher latitudes record higher dispersion (McFadden et al., 1988).

For S_{vand} we filter the original VGP dataset with the Vandamme cut-off (Vandamme, 1994) which applies an iterative VGP cut-off. Applying this VGP filter also reduces the VGP dispersion.

Our results include paleodirections from the Late Neogene, including many from the Brunhes, Matuyama and Gilbert Chrons (see Figure 9. We test whether dispersion varies between chrons by filtering our dataset by age and calculating the dispersion and 95% bootstrap confidence bounds of each separate chron. Our dataset includes a single VGP from the Gauss chron so we exclude this Chron from our calculation. For both filtered and unfiltered VGPs, the dispersion falls within the overlapping 95% bootstrap confidence interval (see supporting information Figure S4), so our dataset suggests there is no distinction in VGP dispersion between chrons.

	S	N_S	S_{45}	N_{S45}	S_{vand}	N_{SVand}
Normal	$30.18^{32.88}_{26.12}$	66	$23.03^{25.81}_{20.84}$	57	$24.27^{29.99}_{20.26}$	59
Reverse	$32.37^{38.04}_{25.52}$	41	$24.37^{27.45}_{21.79}$	36	$24.37^{32.45}_{21.18}$	36
Combined	$30.88^{33.60}_{26.54}$	107	$23.42^{25.69}_{21.38}$	93	$24.17^{28.17}_{21.42}$	95
Brunhes	$32.36^{37.19}_{26.18}$	31	$21.37^{24.52}_{18.90}$	24	$25.98^{37.59}_{18.30}$	28
Matuyama	$31.15^{35.64}_{24.90}$	39	$25.40^{29.83}_{20.29}$	11	$26.06^{31.99}_{22.29}$	36
Gilbert	$30.98^{38.21}_{20.52}$	16	$24.67^{30.56}_{16.85}$	8	$22.08^{39.67}_{17.00}$	14
TK03	$23.35^{27.37}_{20.29}$	107*	$19.68^{21.60}_{18.08}$	107*	$18.76^{21.22}_{16.60}$	107*

Table 6. S: VGP dispersion, S_{45}: VGP dispersion for the data filtered by a 45° VGP cut-off, and S_{vand}:VGP dispersion for the data filtered by the Vandamme cut-off. Beside the VGP dispersion is the bootstrap upper (top) and lower (bottom) 95% confidence bounds for each set of VGPs. *bootstrapped 1000 times.

We compare the results from our dataset to estimates of dispersion from a set of directions drawn from a statistical PSV model, TK03 (Tauxe & Kent, 2004). We drew a set of directions from the centroid position of our sites (78.22°S, 164.34°E), transformed the directions to their corresponding VGPs, and then calculated dispersion for the synthetic dataset. We repeated these steps 1000 times for an S of $24.88\frac{26.30}{23.13}$. The dispersion of our S_{45} and S_{vand} filtered VGPs are consistent with our unfiltered estimate of dispersion from the statistical PSV model TK03. The bounds on the unfiltered VGPs overlap with the bootstrapped 95% confidence interval of our TK03 derived dispersion. Based on our results, dispersion appears consistent between normal and reverse polarities, consistent between the Brunhes and Matuyama chron, and consistent with than VGP dispersion predicted by TK03 (Tauxe & Kent, 2004). We note however that the dispersions for this high latitude study are higher than those predicted by TK03 (although within uncertainty) and that other Giant Gaussian Process models (i.e. Bono et al. (2020), BB18-family) would provide a better fit.

5 Conclusions

We present an extensive study of the paleomagnetic field over the Neogene in the Erebus Volcanic Province, Antarctica (-77.84°, 166.69°) and eleven new $^{40}Ar/^{39}Ar$ results. We recovered a paleopole at 205.6°, 87.1° from 107 independent sites that were subjected to both thermal and AF demagnetization and then filtered using a set of strict selection criteria. The α_{95} of the paleopole is 5.5° and encompasses the spin axis so the paleodirections measured from the EVP during the Neogene are consistent with a GAD field. Additionally, we conducted an IZZI-modified Thellier-Thellier experiment and applied the CCRIT set of selection criteria to estimate paleointensity. Twenty-eight sites passed our criteria and recorded a 33.01 μT $\pm$ 2.59 μT median intensity and a 43.40 ZAm$^2\pm$ 3.41 ZAm^2 median VADM. Compared with global paleointensity estimates stored in the PINT database, our results from Antarctica are lower than expected for a purely GAD field generated by a dipole with the present data value. We conclude that this lower intensity near the pole reflects weaker PDM. However, the possibility remains that there was a strongly non-GAD structure of the paleomagnetic field over the Late Neogene. To test this further, we must repeat this same study of Late Neogene paleomagnetic field at several latitudes (Dossing et al., 2016; Wang et al., 2015) to ensure adequate temporal overlap and high-quality paleointensity results.

Acknowledgments

This work was funded by the National Science Foundation Grants OPP1541285 and EAR1827263. The first author gratefully acknowledges support by the National Science Foundation Graduate Research Fellowship under Grant No. DGE-1650112. We thank the United States Antarctic Program for their ground support in Antarctica. We thank Christeanne Santos for her assistance with data collection and Cathy Constable, Jeff Gee, Shuhui Cai, and Nicole Behar for their helpful discussions. The data are available here

https://earthref.org/MagIC/16912/14bee173-cd18-4c33-858e-de5eab74c528

and will be made public at: https://earthref.org/MagIC/16912 upon acceptance of this manuscript.

References

Aitken, M. J., Allsop, A. L., Bussell, G. D., & Winter, M. B. (1988). Determination of the intensity of the Earth's magnetic field during archeological times: reliability of the Thellier technique. *Rev. Geophys.*, *26*, 3–12.

Behar, N., Shaar, R., Tauxe, L., Asefaw, H., Ebert, Y., Heimann, A., … Hagai, R. (2019). Paleomagnetism and paleosecular variations from the Plio-Pleistocene Golan Heights Volcanic Plateau, Israel. *Geochemistry, Geophysics, Geosystems*, *20*, 4319-4334.

Ben-Yosef, E., Tauxe, L., Levy, T., Shaar, R., Ron, H., & Najjar, M. (2009). Geomagnetic intensity spike recorded in high resolution slag deposit in southern Jordan. *Earth and Planetary Science Letters*, *287*, 529-539.

Biggin, A. (2010). Paleointensity database updated and upgraded. *EOS*, *91*, 15.

Biggin, A., Strik, G., & Langereis, C. (2009). The intensity of the geomagnetic field in the late-Archean: new measurements and analysis of the updated IAGA palaeointensity database. *Earth Planets and Space*, *61*, 9-22.

Bono, R., Biggin, A., Holme, R., Davies, C., Meduri, D., & Bestard, J. (2020). Covariant giant gaussian process models with improved reproduction of paleosecular variation. *Geochem. Geophys. Geosys.*, *21*, e2020GC008960. doi: 10.1029/2020GC008960

Cai, S., Tauxe, L., & Cromwell, G. (2017). Paleointensity from subaerial basltic glasses from the second Hawaii Scientific Drilling Project (HSDP2) core and implications for possible bias in data from lava flow interiors. *J .Geophys. Res.*, *122*, 8664-8674. doi: 10.1002/2017JB014683

Coe, R. (1967). Paleo-intensities of the Earth's magnetic field determined from Tertiary and Quaternary rocks. *Journal of Geophysical Research*, *72*(12), 3247-3262.

Constable, C., Korte, M., & Panovska, S. (2016). Persistent high paleosecular variation activity in southern hemisphere for at least 10,000 years. *Earth and Planet. Sci. Lett.*, *453*, 78-86.

Cox, A. (1970). Latitude dependence of the angular dispersion of the geomagnetic field. *Geophys. J. Roy. Astron. Soc*, *20*, 253-269.

Creer, K. (1967). *Thermal demagnetization by the continuous method.* Chapman and Hall.

Cromwell, G., Tauxe, L., Constable, C., & Jarboe, N. (2018). PSV10: A global dataset for 0-10 Ma time-averaged field and paleosecular variation studies. *Geochemistry, Geophysics, Geosystems*, *19*, 1533-1558.

Cromwell, G., Tauxe, L., Staudigel, H., & Ron, H. (2015). Paleointensity estimates from historic and modern Hawaiian lava flows using basaltic volcanic glass as a primary source material. *Phys. Earth Planet. Int.*, *241*, 44-56.

Cromwell, G., Trusdell, F., Tauxe, L., Staudigel, H., & Ron, H. (2018). Holocene paleointensity of the island of Hawai'i from glassy volcanics. *Geochem. Geophys. Geosys.*, *19*, 3224-3245. doi: 10.1002/2017GC006927

Dodson, M., & McClelland-Brown, E. (1980). Magnetic blocking temperatures of single-domain grains during slow cooling. *Journal of Geophysical Research*, *85*, 2625-2637.

Dossing, A., Muxworthy, A., Supakulopas, R., Riishuus, M., & Mac Niocaill, C. (2016). High northern geomagnetic field behavior and new constraints on the Gilsa event: Paleomagnetic and ^{40}Ar/^{39}Ar. *Earth and Planetary Science Letters*, *456*, 98-111.

Dunlop, D., & Özdemir, O. (2001). Beyond Néel's theories: thermal demagnetization of narrow-band partial thermoremanent magnetization. *Phys. Earth Planet. Int.*, *126*, 43-57.

Dunlop, D., Zhang, B., & Özdemir, O. (2005). Linear and nonlinear thellier paleointensity behavior of natural minerals. *Journal of Geophysical Research*, *110*, B01103. doi: https://doi.org/10.1029/2004JB003095

Fisher, R. A. (1953). Dispersion on a sphere. *Proc. Roy. Soc. London, Ser. A*, *217*, 295–305.

Fox, J., & Aitken, M. (1980). Cooling-rate dependence of thermoremanent magnetisation. *Nature*, *283*, 462-463.

Gilbert, W. (1958). *On the Magnet, Facsimile of 1900 translation by Silvanus P. Thompson and the Gilbert Club.* New York: Basic Books, Inc.

Glatzmaier, G., & Coe, R. (2007). Magnetic polarity reversals in the core. In *Core dynamics* (Vol. 5, p. 283-297). Elsevier.

Gradstein, F., Ogg, J., Schmitz, M., & Ogg, G. (2012). *Geologic time scale 2012.* Amsterdam: Elsevier.

Halgedahl, S., & Fuller, M. (1980). Magnetic domain observations of nucleation processes in fine particles of intermediate titanomagnetite. *Nature*, *288*, 70-72.

Harrison, R., & Feinberg, J. (2008). An improved algorithm for calculating first-order reversal curve distributions using locally weighted regression smoothing. *Geochemistry Geophysics Geosystems*, *9*, Q05016. doi: doi:10.1029/2008GC001987

Heaton, D., & Koppers, A. (2019). High-resolution ^{40}Ar/^{39}Ar geochronology of the Louisville Seamounts IODP Expedition 330 drill sites: Implications or the dduration of hot spot-related volcanism and age progressions. *Geochemistry, Geophysics, Geosystems*, *46*, 4073-4102. doi: 10.1029/2019GL083542

Hoffman, K., & Biggin, A. (2005). A rapid multi-sample approach to the determination of absolute paleointensity. *J. Geophys. Res.*, *110*, B12108.

Holme, R. (2007). Large-scale flow in the core. In *Core dynamics* (Vol. 5, p. 107-130). Elsevier.

Irving, E., Robertson, W., Stott, P., Tarling, D., & Ward, M. (1961). Treatment of partially stable sedimentary rocks showing planar distribution of directions of magnetization. *Journal of Geophysical Research*, *66*(6).

Jackson, A., & Finlay, C. (2007). Geomagnetic secular variation and its applications to the core. In *Geomagnetism* (Vol. 5, p. 147-193). Elsevier.

Jackson, A., Jonkers, A. R. T., & Walker, M. R. (2000). Four centuries of geomagnetic secular variation from historical records. *Phil Trans Roy Soc London, Series A*, *358*(1768), 957-990.
Johnson, C. L., Constable, C. G., Tauxe, L., Barendregt, R., Brown, L., Coe, R., ... Stone, D. (2008). Recent investigations of the 0-5 Ma geomagnetic field recorded in lava flows. *Geochemistry, Geophysics, Geosystems*, *9*, Q04032. doi: doi:10.1029/2007GC001696
Juarez, T., Tauxe, L., Gee, J. S., & Pick, T. (1998). The intensity of the earth's magnetic field over the past 160 million years. *Nature*, *394*, 878-881.
Kirschvink, J. L. (1980). The least-squares line and plane and the analysis of paleomagnetic data. *Geophys. Jour. Roy. Astron. Soc.*, *62*, 699–718.
Kissel, C., & Laj, C. (2004). Improvements in procedure and paleointensity selection criteria (PICRIT-03) for Thellier and Thellier determinations: Application to Hawaiian basaltic long cores. *Physics of the Earth and Planetary Interiors*, *147*, 155-169.
Koppers, A. (2003). High-resolution ^{40}Ar/^{39}Ar dating of the oldest oceanic basement basalts in the western Pacific basin. *Geochem. Geophys. Geosys.*, *4*, doi:10.1029/2003GC000574.
Koppers, A., Russell, J., Jackson, M., Konter, J., Staudigel, H., & Hart, S. (2008). Samoa reinstated as a primary hotspot trail. *Geology*, *36*, 435-438, doi:10.1130/G24630A.1.
Koppers, A., Staudigel, H., & Wijbrans, J. (2000). Dating crystalline groundmass separates of altered Cretaceous seamount basalts by the ^{40}Ar/^{39}Ar incremental heating technique. *Chem. Geol*, *166*, 139-158.
Lawrence, K. P., Tauxe, L., Staudigel, H., Constable, C., Koppers, A., McIntosh, W. C., & Johnson, C. L. (2009). Paleomagnetic field properties near the southern hemisphere tangent cylinder. *Geochem. Geophys. Geosyst.*, *10, Q01005*, doi:10.1029/2008GC00207.
Leonhardt, R., Heunemann, C., & Krasa, D. (2004). Analyzing absolute paleointensity determinations: Acceptance criteria and the software thelliertool4.0. *Geochemistry, Geophysics, Geosystems*, *5*.
Livermore, P., Fournier, A., & Gallet, Y. (2014). Core-flow constraints on extreme archeomagnetic intensity changes. *Earth and Planet. Sci. Lett.*, *387*, 145-156. doi: 10.1016/j.epsl.2013.11.020
Lowes, F. (1973). Spatial power spectrum of the main geomagnetic field, and extrapolation to the core. *Geophysical Journal of the Royal Astronomical Society*, *36*, 717-730.
Mankinen, E., & Cox, A. (1988). Paleomagnetic investigation of some volcanic rocks from the McMurdo Volcanic Province, Antarctica. *Journal of Geophysical Research*, *93*(B10), 11599-11612.
McElhinny, M. (1973). *Paleomagnetism and plate tectonics.* Cambridge: Cambridge University Press.
McElhinny, M. (2007). Encyclopedia of Geomagnetism and Paleomagnetism. In D. Gubbins & E. Herrero-Bervera (Eds.), (chap. Geocentric Axial Dipole Hypothesis). Springer-Verlag. doi: https://doi.org/10.1007/978-1-4020-4423-6_107
McElhinny, M., & Lock, J. (1996). IAGA paleomagnetic databases with access. *Surveys in Geophysics*, *17*(5), 575-591.
McFadden, P. L., & Mcelhinny, M. (1982). Variations in the geomagnetic dipole 2: statistical analysis of VDMs for the past 5 m.y. *J. Geomag. Geoelctr.*, *34*, 163-189.
McFadden, P. L., Merrill, R. T., & McElhinny, M. W. (1988). Dipole/quadrupole family modeling of paleosecular variation. *J. Geophys. Res*, *93*, 11583-11588.
Nagata, T., Arai, Y., & Momose, K. (1963). Secular variation of the geomagnetic total force during the last 5000 years. *J. Geophys. Res.*, *68*, 5277-5282.

Néel, L. (1955). Some theoretical aspects of rock-magnetism. *Adv. Phys*, *4*, 191-243.

Opdyke, N., & Henry, K. (1969). A test of the dipole hypothesis. *Earth and Planetary Science Letters*, *6*, 139-151.

Paterson, G. (2011). A simple test for the presence of multidomain behavior during paleointensity experiments. *Journal of Geophysical Research*, *116*, B10104.

Paterson, G., Tauxe, L., Biggin, A., Shaar, R., & Jonestrask, L. (2014). On improving the selection of Thellier-type paleointensity data. *Geochemistry Geophysics Geosystems*, *15*(4). doi: 10.1002/2013GC005135

Pike, C., Roberts, A., & Verosub, K. (1999). Characterizing interactions in fine magnetic particle systems using first order reversal curves. *J. Appl. Phys.*, *85*, 6660-6667.

Pike, C., Roberts, A., & Verosub, K. (2001). First-order reversal curve diagrams and thermal relaxation effects in magnetic particles. *Geophysical Journal International*, *145*, 721-730.

Roberts, C., A.P.and Pike, & Verosub, K. (2000). First-order reversal curve diagrams: A new tool for characterizing the magnetic properties of natural samples. *Journal of Geophysical Research*, *106*, 28461-28475.

Santos, C., & Tauxe, L. (2019). Investigating the accuracy, precision, and cooling rate dependence of laboratory-acquired thermal remanences during paleointensity experiments. *Geochemistry, Geophysics, and Geosystems*, *20*, 383-397.

Selkin, P., Gee, J., & Tauxe, L. (2007). Nonlinear thermoremanence acquisition and implications for paleointensity data. *Earth and Planetary Science Letters*, *256*, 81-89.

Selkin, P., & Tauxe, L. (2000). Long-term variations in paleointensity. *Phil. Trans. Roy. Soc. Lond.*, *358*, 1065-1088.

Shaar, R., & Tauxe, L. (2013). Thellier_gui: An integrated tool for analyzing paleointensity data from thellier-type experiments. *Geochem. Geophys. Geosys.*, *14*, 677-692.

Shashkanov, V., & Metallova, V. (1972). Violation of Thellier's law for partial thermoremanent magnetizations. *Izv. Earth Physics*, *3*, 80-86.

Shaw, J. (1974). A new method of determining the magnitude of the paleomagnetic field application to 5 historic lavas and five archeological samples. *Geophys. J. R. Astron. Soc.*, *39*, 133-141.

Shcherbakov, V., McClelland, E., & Shcherbakova, V. (1993). A model of multidomain thermoremanent magnetization incorporating temperature-variable domain structure. *J. Geophys. Res*, *98*(B4), 6201-6214.

Smirnov, A. V., & Tarduno, J. A. (2003). Magnetic hysteresis monitoring of Cretaceous submarine basaltic glass during Thellier paleointensity experiments: evidence for alteration and attendant low field bias. *Earth Planet. Sci. Lett.*, *206*(3-4), 571-585.

Stephenson, A. (1967). *Apparatus for the thermal demagnetization by the progressive method.* Chapman and Hall.

Tanaka, H., & Kobayashi, T. (2003). Paleomagnetism of the late Quaternary Ontake Volcano, Japan: directions, intensities, and excursions. *Earth Planets and Space*, *55*(4), 189-202.

Tanaka, H., Kono, M., & Uchimura, H. (1995). Some global features of paleointensity in geological time. *Geophys. J. Int.*, *120*, 97–102.

Tauxe, L., Gans, P., & Mankinen, E. (2004). Paleomagnetism and ^{40}Ar/^{39}Ar ages from volcanics extruded during the Matuyama and Brunhes Chrons near McMurdo Sound, Antarctica. *Geochemistry Geophysics Geosystems*, *5*(6).

Tauxe, L., Gee, J., Steiner, M., & Staudigel, H. (2013). Paleointensity results from the Jurassic: New constraints from submarine basaltic glasses of ODP Site 801C. *Geochemistry Geophysics Geosystems*, *14*(10). doi: 10.1002/ggge/20282

Tauxe, L., & Kent, D. V. (2004). A simplified statistical model for the geomagnetic field and the detection of shallow bias in paleomagnetic inclinations: Was the ancient magnetic field dipolar? In e. a. Channell J.E.T. (Ed.), *Timescales of the paleomagnetic field* (Vol. 145, p. 101-116). Washington, D.C.: American Geophysical Union.

Tauxe, L., N., K., & Constable, C. (1991). Bootstrap statistics for paleomagnetic data. *Journal of Geophysical Research*, *96*, 11723-11740.

Tauxe, L., Shaar, R., Jonestrask, L., Swanson-Hysell, N., Minnett, R., Koppers, A. A. P., … Fairchild, L. (2016). PmagPy: Software package for paleomagnetic data analysis and a bridge to the Magnetics Information Consortium MagIC) database. *Geochem. Geophys. Geosys.*, *17*. doi: 10.1002/2016GC006307

Tauxe, L., & Staudigel, H. (2004). Strength of the geomagnetic field in the Cretaceous Normal Superchron: New data from submarine basaltic glass of the Troodos Ophiolite. *Geochem. Geophys. Geosyst.*, *5*(2), Q02H06, doi:10.1029/2003GC000635.

Tauxe, L., & Yamazaki, T. (2015). Paleointensities. In M. Kono (Ed.), *Geomagnetism* (2nd Edition ed., Vol. 5, p. 461-509). Elsevier.

Thébault, E., Finlay, C., Beggan, C., Alken, P., Aubert, J., Barrois, O., … Lowes, F. (2015). International Geomagnetic Reference Field: the 12th generation. *Earth, Planets, and Space*, *67*, 67-79. doi: 10.1186/s40623-015-0228-9

Thellier, E. (1938). Sur l'aimantation des terres cuites et ses applications géophysique. *Ann. Inst. Phys. Globe Univ. Paris*, *16*, 157-302.

Thellier, E., & Thellier, O. (1959). Sur l'intensité du champ magnétique terrestre dans le passé historique et géologique. *Ann. Geophys.*, *15*, 285–378.

Vandamme, D. (1994). A new method to determine paleosecular variation. *Phys. Earth Planet. Int.*, *85*, 131-142.

Walton, D., & Shaw, J. (1922). Microwave demagnetization. *Journal of Applied Physics*, *71*, 1549.

Wang, H., Kent, D., & Rochette, P. (2015). Weaker axially dipolar time-averaged paleomagnetic field based on multidomain-corrected paleointensities from Galapagos lavas. *Proc. Nat. Acad. Sci.*, *112*, 15036-15041. doi: 10.1073/pnas.1505450112

Watkins, N. (1973). Brunhes epoch geomagnetic secular variation on Reunion Island. *Journal of Geophysical Research*, *78*(32), 7763-7768.

Yu, Y., Tauxe, L., & Genevey, A. (2004). Toward an optimal geomagnetic field intensity determination technique. *Geochemistry, Geophysics, Geosystems*, *5*.

Ziegler, L., Constable, C., Johnson, C. L., & Tauxe, L. (2011). PADM2M: a penalized maximum likelihood model of the 0-2 Ma palaeomagnetic axial dipole moment. *Geophys. J. Int.*.

Zijderveld, J. D. A. (1967). *A.C. demagnetization of rocks: analysis of results.* Chapman and Hall.

Supporting Information for "Four Dimensional Paleomagnetic Dataset: Late Neogene paleodirection and paleointensity Results from the Erebus Volcanic Province, Antarctica"

H.A. Asefaw[1], L. Tauxe[1], A.A.P. Koppers [2], H. Staudigel[1]

[1]Scripps Institution of Oceanography, University of California

[2]College of Earth, Ocean and Atmospheric Sciences

Contents of this file

New Site	Combined Sites
mc1301	mc1012, mc1203
mc1302	mc1013, mc1204
mc1303	mc1026, mc1129
mc1304	mc1049, mc1104
mc1305	mc1050, mc1105
mc1306	mc1161, mc1162
mc1307	mc1166, mc1219

Table S1. Several lava flows that were considered separate sites from the original study recover identical paleodirections. Field examination suggests that these sites likely sample the same event, so we combined the original sites, listed in the combined sites column, into a single site.

Table S2. Plateau age, normal isochron age, inverse isochron age, and total fusion age results from the $^{40}Ar/^{39}Ar$ incremental heating method used for geochronology.

Figure S1. A representative outcrop containing the original drill cores of Lawrence et al. 2009 sampled from the interior of the lava flow and the hand samples collected for this study from the lava flow top.

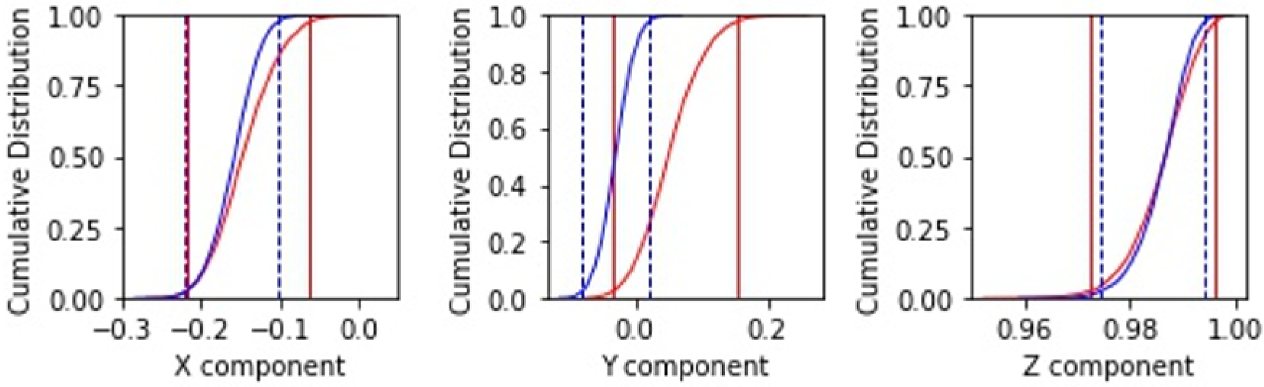

Figure S2. The results of the bootstrap reversal test applied to the normal and reverse directions. A bootstrap approach is applied by resampling 1000 normal directions, calculating their mean direction and then repeating this procedure 1000 times. The results of the mean normal directions (blue) and the mean reverse directions (red) are displayed as cumulative distribution functions of the x-component (left), y-component (center), and z-component(right) of the mean directions. The corresponding 95% confidence bounds for the normal (vertical red lines) and reverse (vertical blue lines) directions.

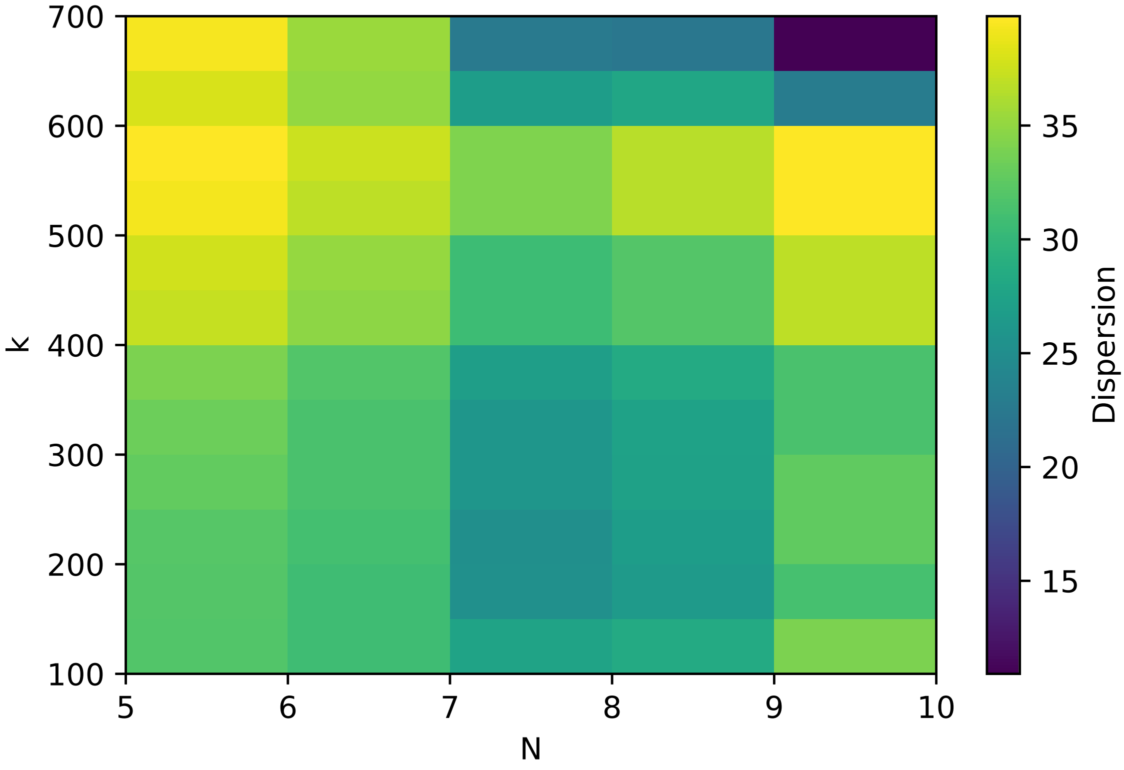

Figure S3. A heat map of dispersion calculated from our combined normal and reverse polarity directions that was filtered by different combinations of N, the number of cores, and k, the precision parameter.

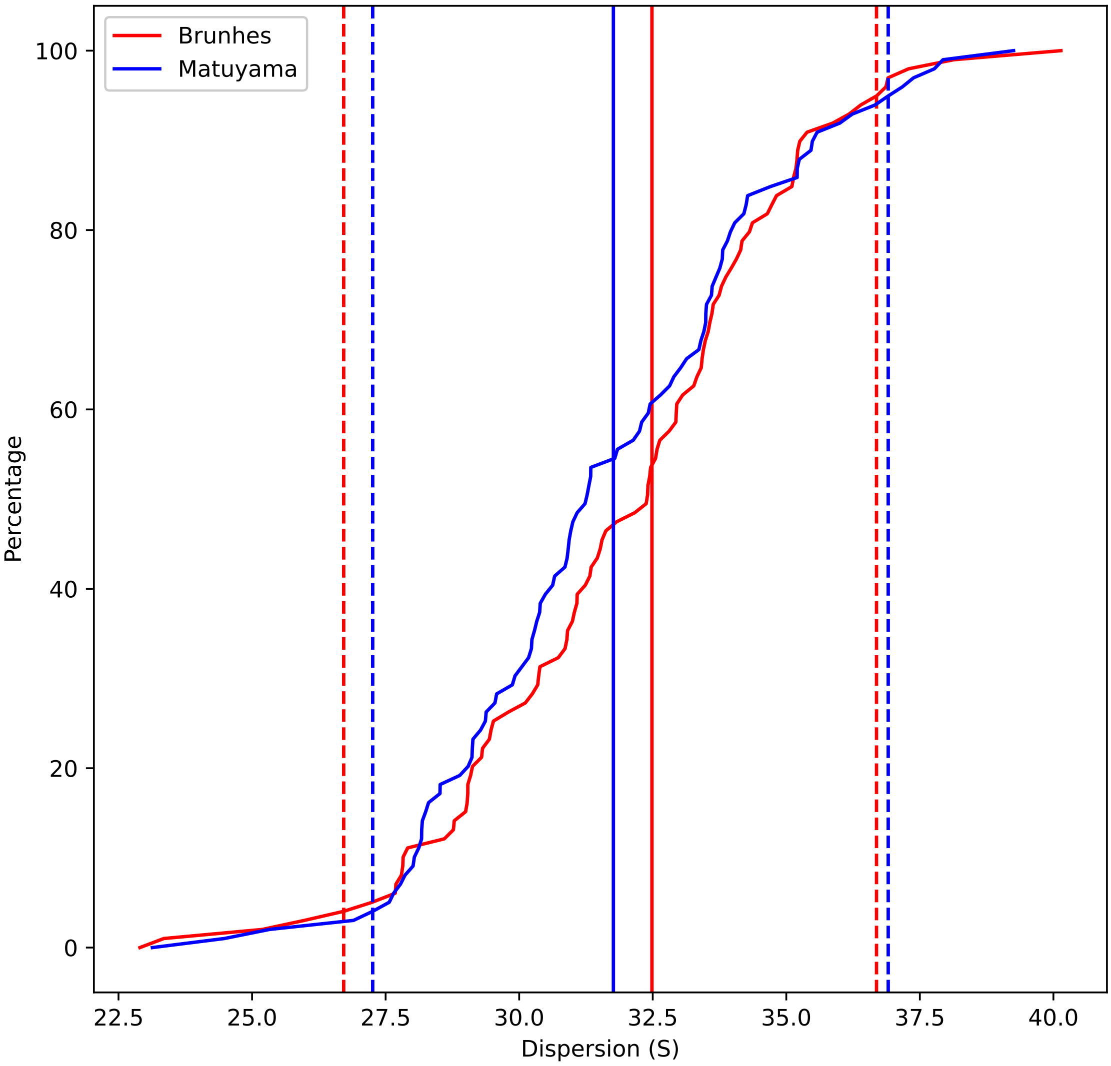

Figure S4. The CDF (cumulative distribution function) of dispersion (S) for 1000 bootstrap subsets of our Brunhes (red) and Maytuyama (blue) datasets. The 95% confidence bounds are marked as vertical dashed lines.

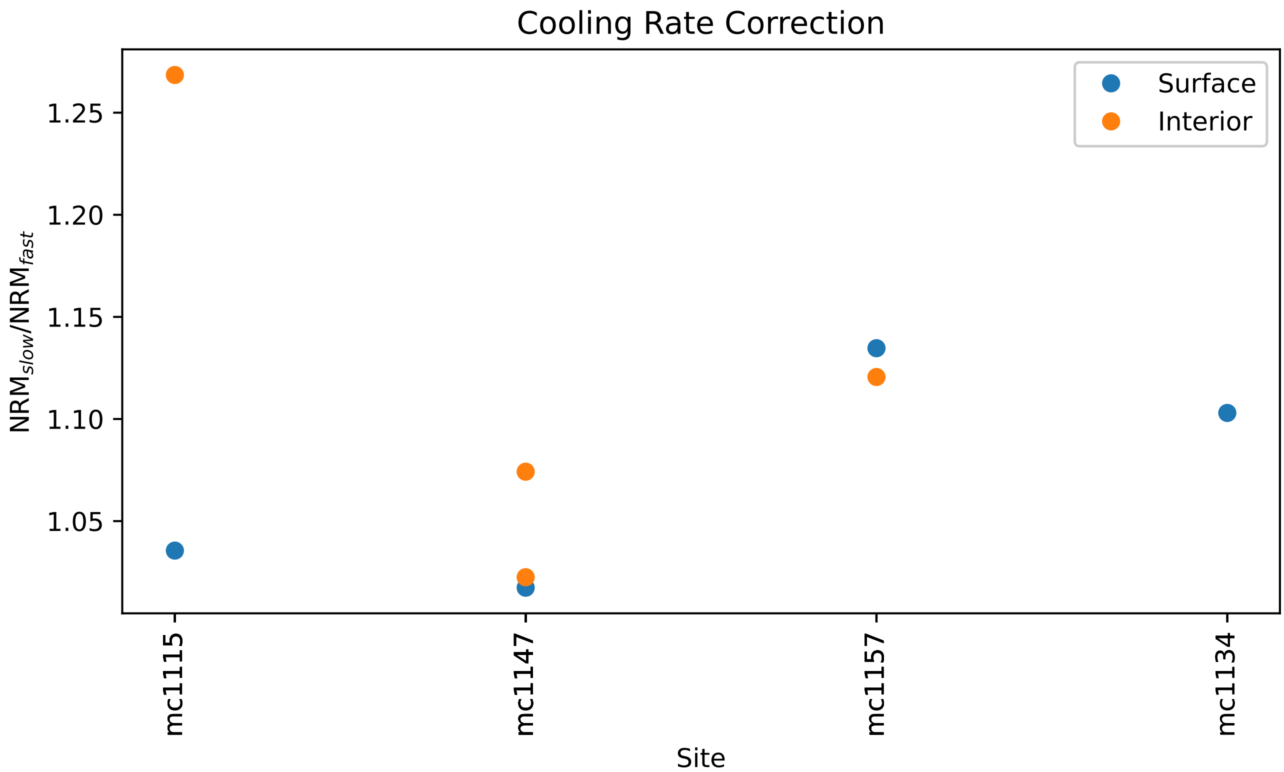

Figure S5. The results of the cooling rate experiment. Each specimen requires a cooling rate correction ranging from 2% to 27%, but the correction for the specimen from the interiors equals (mc1157) or exceeds (mc1115, mc1147) the cooling rate correction required for the specimen from the surface of the same lava flow.

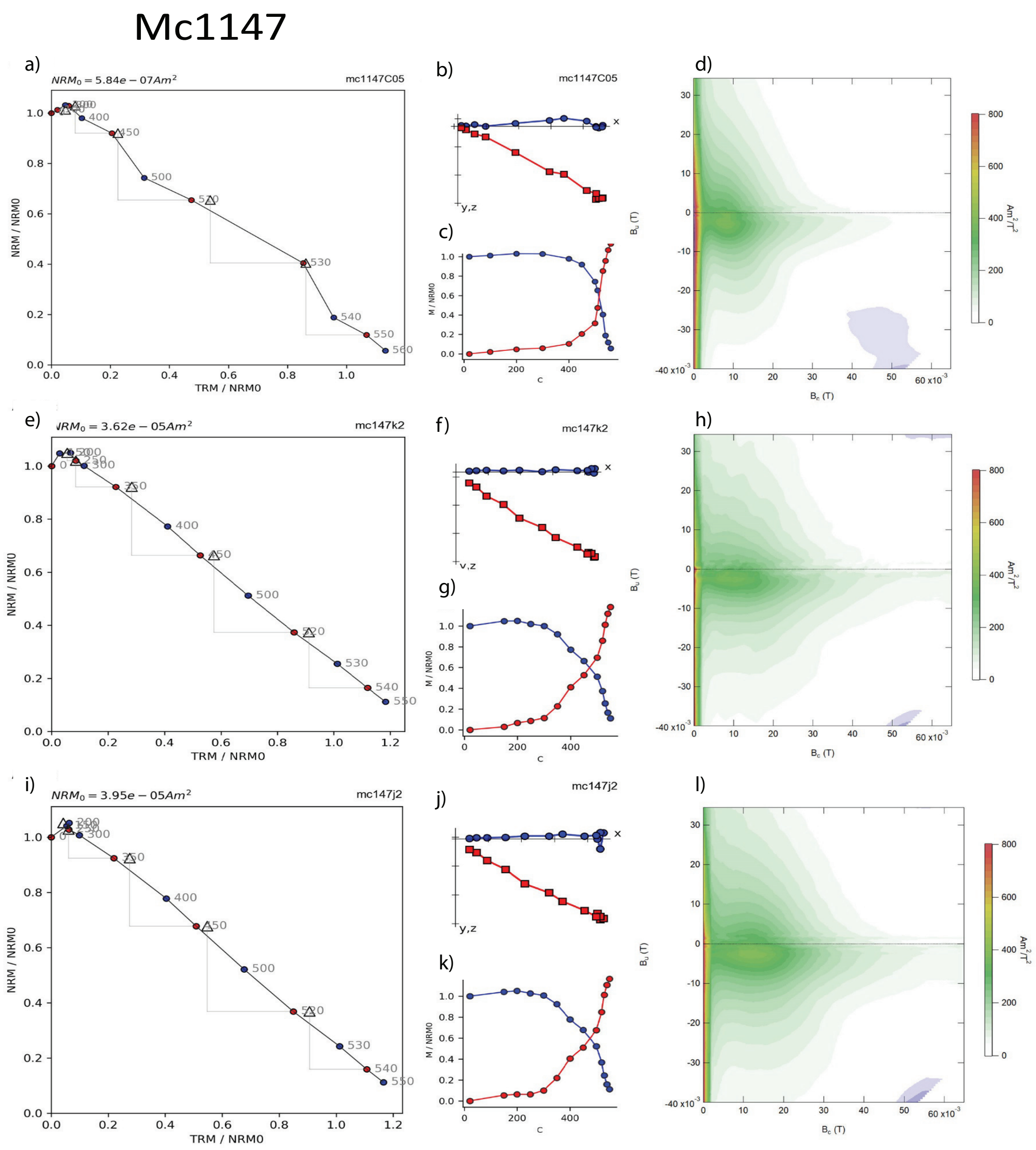

Figure S6. Arai diagram (a,e,i), zijderveld diagram (b, f, j), MT curve (c,g, k), and FORC diagrams (d,h,l) for samples from site mc1147 that passed CCRIT. Specimen mc1147C05 (a - d) was sampled from the lava flow top and yielded a 25.8T paleointensity; mc147k2 (e-h) was collected from the lava flow interior and estimated a 21.1T paleointensity; mc147j2 (i-l) was sampled from the lava flow interior and yielded a 21.3T

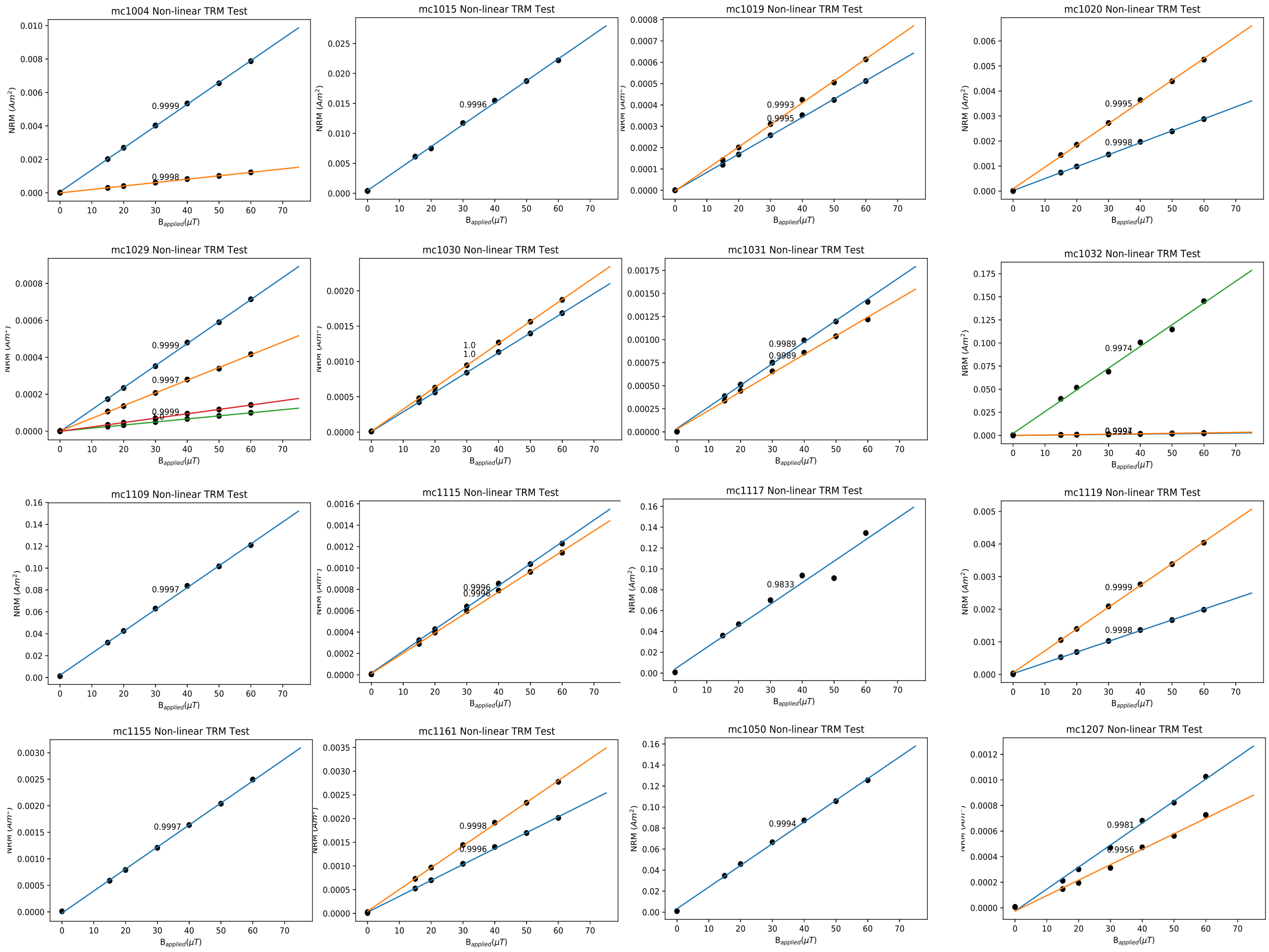

Figure S7. Results of the non-linear TRM acquisition test. Specimen are grouped by site, each line is a successful specimen from that site. The best fit line for each specimen is plotted along with its correlation coefficient.